Mon. Not. R. Astron. Soc. **269**, 785–813 (1994)

Line-of-sight velocity distributions of elliptical galaxies

R. Bender,[1,2]★ R.P. Saglia[1,2,3] and O.E. Gerhard[1]

[1] *Landessternwarte, Königstuhl, D-69117 Heidelberg, Germany*
[2] *Present address: Institut für Astronomie und Astrophysik, Scheinerstr. 1, D-81679 München, Germany*
[3] *Dipartimento di Matematica, Università di Pisa, I-56157 Pisa, Italy*

Accepted 1994 March 18. Received 1994 March 18; in original form 1993 December 13

ABSTRACT

The line-of-sight velocity distributions (LOSVDs) have been measured to $> R_e/2$ along the major axes of 44 elliptical galaxies (more than 80 per cent of all ellipticals north of $\delta = -10°$ and brighter than $B_T = 12.0$), together with stellar rotational velocity and velocity dispersion profiles. For 19 of these 44 objects, minor axis profiles are also given. Monte Carlo simulations have been used to estimate errors. LOSVDs are found to deviate from Gaussians by no more than ≈ 10 per cent.

If rotation is present, LOSVDs are asymmetric with the prograde wings being always steeper than the retrograde wings. The degree of asymmetry (measured by the H_3 Gauss-Hermite coefficient) correlates with v/σ. Round and boxy ellipticals have lower asymmetries than flat and discy ones. On the whole, both types must have intrinsically asymmetric velocity distributions. Symmetric deviations (measured by the H_4 Gauss-Hermite coefficient) are generally smaller than asymmetric ones.

On the basis of the observed LOSVD shapes, the validity of two-integral models can be ruled out for most of the *non-discy* objects observed here (discy ellipticals require detailed modelling before similar conclusions can be drawn). Discy ellipticals have H_3 and H_4 major and minor axis profiles which appear consistent with a bulge+disc superposition. The observed H_4 profile in M87 argues for radially anisotropic spherical or oblate models.

Velocity dispersion profiles show significant individuality, but typically become flat outside $R_e/4$. Major and minor axis slopes are mostly correlated one to one. We confirm that, with increasing luminosity, ellipticals become more anisotropic and that discy ellipticals have more rotational support.

The Fundamental Plane of elliptical galaxies is tighter if total kinetic energy is used instead of central velocity dispersion. Both the small scatter about the Fundamental Plane and the homogenous and systematic properties of the LOSVDs imply that only a small range of dynamical models is realized in elliptical galaxies.

Key words: galaxies: elliptical and lenticular, cD – galaxies: fundamental parameters – galaxies: individual: M87 – galaxies: kinematics and dynamics.

1 INTRODUCTION

The understanding of the dynamics of elliptical galaxies remains incomplete with the sole knowledge of velocity dispersion and rotation profiles, even if available along many slit positions. As has long been known, the possibility of velocity dispersion anisotropy introduces a degeneracy that prohibits any straightforward deprojection of observed quantities.

The classical example for this degeneracy is provided by the study of the central dynamics of M87. The observed central rise in velocity dispersion and density was originally interpreted as being caused by a nuclear black hole (Sargent et al. 1978). However, this conclusion was based on the assumption of isotropic velocity dispersions. Binney & Mamon (1982) showed that, by allowing for radially varying anisotropy, it is possible to construct a model that fits the data with radially constant mass-to-light ratio and no need for a black hole. Such radially anisotropic models are prone to instabilities (Merritt 1987), but it would be nearly impossible to construct and test for stability all possible models consistent with the velocity dispersion data. Clearly, a better understanding of the central dynamics of M87 and many other black hole candidates (e.g. Kormendy 1993) requires more observational constraints.

★ Visiting Astronomer of the German-Spanish Astronomical Center, Calar Alto, operated by the Max Plank Institut für Astronomie, Heidelberg, jointly with the Spanish National Commission for Astronomy.

Other important problems of stellar dynamics that are greatly affected by anisotropy and yet ill understood are: Are elliptical galaxies surrounded by dark haloes (Kent 1990; Saglia et al. 1993a; Bertola et al. 1993)? What are the typical shapes of ellipticals (Franx, Illingworth & de Zeeuw 1991; Saglia, Bender & Dressler 1993b)? How are their distribution functions built (e.g. Dehnen & Gerhard 1993)? and Why do ellipticals follow very tight scaling relations between central velocity dispersion and photometric parameters (the 'Fundamental Plane', see Djorgovski & Davis 1987; Faber et al. 1987; Bender, Burstein & Faber 1992) despite potentially large variations in the central velocity dispersion relative to the mean kinetic energy? The latter questions also have implications for the formation scenario.

Recent progress in observational techniques and analytical tools on the one hand (Bender 1990; Rix & White 1992; van der Marel & Franx 1993; Winsall & Freeman 1993; Kuijken & Merrifield 1993; Saha & Williams 1994), and in theoretical insight on the other hand (Dejonghe 1987; Merrifield & Kent 1990; Gerhard 1991, 1993; Dejonghe & Merritt 1992; Merritt 1993; Dehnen & Gerhard 1993, 1994; Evans 1993, 1994) have indicated a potential way out of the degeneracy caused by anisotropy. The hope is that if, in addition to rotational velocity v and dispersion σ, more detailed information on the line-of-sight velocity distribution can be inferred (i.e. skewness, kurtosis), it may be possible to constrain anisotropy in such a way that the associated degeneracy problem may be solved.

First successes in measuring the shapes of line-of-sight velocity distributions (hereafter LOSVDs) mainly concerned asymmetries because these turned out to be rather easily detectable (Franx & Illingworth 1988; Bender 1990; Wagner, Dettmar & Bender 1989; Rix & White 1992; van der Marel & Franx 1993; Cinzano & van der Marel 1993; Kuijken & Merrifield 1993). Asymmetries were detected in ellipticals that showed evidence for a two-component structure (discy ellipticals, ellipticals with peculiar core kinematics). In these objects one of the components has high v/σ and therefore, even if the LOSVD of each component is symmetric, their superposition will appear asymmetric†.

On the other hand, progress in measuring symmetric deviations was rather slow, mainly because symmetric deviations appear to be small compared to asymmetric ones and their reliability is more difficult to assess. Basically, only upper limits on deviations from Gaussian line profiles could be derived (Winsall & Freeman 1993; van der Marel & Franx 1993).

As becomes clear from this review of the literature, only a few ellipticals (and not necessarily representative ones) have so far been analysed for deviations from Gaussian LOSVDs. In this paper we present for the first time LOSVDs for a large and unbiased sample of ellipticals. The sample contains more than 80 per cent of all ellipticals north of $\delta = -10°$ and brighter than $B_T = 12.0$, plus additional objects selected in order to represent different types of objects in sufficient numbers. We characterize the deviations from Gaussian line shapes by Gauss-Hermite functions as has been proposed by Gerhard (1993) and van der Marel & Franx (1993). This parametrization is advantageous compared to measuring standard higher order moments because these depend strongly on the wings of the LOSVDs which are most uncertain.

The aim of this paper is two-fold. First, we want to provide an overview of the variety of line-of-sight velocity distributions observed in ellipticals. Secondly, we want to isolate characteristic sub-groups of which proto-typical objects can be studied in more detail in the future. The paper is organized as follows: Section 2 describes the observations, Section 3 the reductions and error estimates, and Sections 4 and 5 the results. In Section 6 we draw conclusions.

2 OBSERVATIONS

The observations were carried out between 1987 and 1991 with the 2.2-m and 3.5-m telescopes on Calar Alto, Spain. The spectrographs used were a Boller & Chivens longslit spectrograph and a Boller & Chivens longslit twin spectrograph (Solf 1983). In all observations a 1200 line mm^{-1} grating was used, giving dispersions between 36 and 60 Å mm^{-1}. The detector was a RCA CCD with 15-μm pixel size. Slit widths ranged between 1.4 arcsec and 3.7 arcsec which in turn yielded velocity resolutions between $\sigma_I = 40$ km s^{-1} (FWHM= 90 km s^{-1}) and $\sigma_I = 70$ km s^{-1} (FWHM= 160 km s^{-1}). For further information, see Table 1.

The seeing during the observations ranged between 1 arcsec and 2.5 arcsec. Since our interest was focused on the kinematics of the main bodies of the galaxies (and less on cores), most spectra were binned to somewhat larger than the seeing FWHM during read-out in order to minimize degrading of the signal-to-noise ratio due to read-out noise. Typically, two spectra per slit position on the galaxy were obtained with summed exposure times ranging between 1 h and 3 h (see Table 2 for a detailed listing).

During each observing run, template stars of type G8III to K5III were observed and trailed along and across the slit; this ensured that the instrumental broadening was always the same in the stars as in the galaxies. No significant change in the instrumental broadening was noticed over the slit range over which the galaxies extended. Also flexure of the spectrographs was found to be negligible. Both dome and twilight flatfields were taken in order to allow accurate flatfielding.

3 REDUCTION AND ERROR ESTIMATES

The aim of this paper is to provide information on LOSVDs for a large and unbiased sample of elliptical galaxies. In accordance with van der Marel & Franx (1993) we will describe the LOSVDs $f(v)$ by a Gaussian plus third- and fourth-order Gauss-Hermite functions:

$$f(v) = I_0 \exp(-\frac{y^2}{2}) (1 + H_3\mathcal{H}_3(y) + H_4\mathcal{H}_4(y)) \quad (1)$$

with $y = (v - v_{\rm fit})/\sigma_{\rm fit}$, and where

$$\mathcal{H}_3(y) = (2\sqrt{2}y^3 - 3\sqrt{2}y)/\sqrt{6} \quad (2)$$

$$\mathcal{H}_4(y) = (4y^4 - 12y^2 + 3)/\sqrt{24} \quad (3)$$

are the standard Hermite polynomials, $u_i = \exp(-y^2/2) \times \mathcal{H}_i(y)$ are the Gauss-Hermite basis functions, and H_3 and H_4 are their amplitudes. I_0 is a normalization constant. Fig. 1 shows a Gaussian and the corresponding Gauss-Hermite

† Unlike in the case of disc galaxies, the v/σ of ellipticals is not high enough for projection alone to cause asymmetries, e.g. Bender (1990).

Table 1. Set-up of the observing runs.

Run #	Date	Telescope	Instrument	Detector	Wavelength Range (Å)	Resolution km s^{-1}	Scale ($''$pixel^{-1})	Slit width ($''$)
1	2.19.1987-2.28.1987	CA 3.5	B&C	RCA 15μm	4650-5550	70	2.24	1.7
2	6.17.1987-6.23.1987	CA 2.2	B&C	RCA 15μm	4650-5550	60	3.6	3.0
3	7.1.1987-7.6.1987	CA 3.5	B&C	RCA 15μm	4650-5550	70	2.24	1.8
4	1.20.1988-1.25.1988	CA 2.2	B&C	RCA 15μm	4650-5550	70	3.6	3.7
5	1.20.1988-1.24.1988	CA 3.5	B&C	RCA 15μm	4650-5550	70	2.24	1.8
6	3.6.1989-3.16.1989	CA 2.2	B&C	RCA 15μm	4650-5550	55	2.7	2.7
7	7.3.1989-7.10.1989	CA 3.5	Twin	RCA 15μm	4890-5430	46	2.24	2.1
8	3.6.1990-3.11.1990	CA 3.5	Twin	RCA 15μm	4890-5430	46	1.68	2.1
9	3.11.1991-3.11.1991	CA 3.5	Twin	RCA 15μm	4830-5400	35	0.56	1.4
10	3.12.1991-3.18.1991	CA 3.5	Twin	RCA 15μm	4890-5430	46	0.56	2.1

functions of third and fourth order, which for the purpose of illustration were chosen to have amplitudes of 0.1 of the Gaussian. Asymmetric LOSVDs with prograde wings steeper than retrograde ones are obtained for $H_3 < 0$, 'triangular' LOSVDs with $H_4 > 0$ and flat-top LOSVDs with $H_4 < 0$. Higher order terms have not been considered in equation (1), because their determination requires spectra of signal-to-noise ratio larger than we normally have.

The following subsections will describe how the LOSVD and the parameters $v_{\rm fit}$, $\sigma_{\rm fit}$, H_3, H_4 were extracted from the spectra and how their errors were estimated.

3.1 Reduction and derivation of line-of-sight velocity distributions

The CCD spectra were de-biased, dark-subtracted and flat-fielded in the usual way. Hot pixels and cosmic ray events were removed with a $\kappa-\sigma$-clipping procedure. Then, the spectra were rebinned to a logarithmic wavelength scale and the mean sky spectrum during each exposure was derived by averaging several lines from the edges of the CCD spectra. After subtraction of the sky spectra, spectra of the same galaxy taken at identical slit positions were centred and added. Then, the spectra were rebinned along the slit in order to guarantee a signal-to-noise ratio that allowed the derivation of kinematic parameters. As the final step of the pre-processing, the galaxy continuum was removed in two steps. First, a fourth- to sixth-order polynomial was fitted to each line-by-line spectrum. Then, the rms variation σ_s of the spectrum around the fitted polynomial was calculated and the fit was repeated including only those pixels of which the value fell in a range between $0\sigma_s$ and $2\sigma_s$ around the first fit. Finally, the spectrum was divided by this second fit polynomial. This procedure avoids the fact that the stronger absorption lines disturb the fit and leads to a satisfactory approximation of the galaxy 'continuum'. This method of continuum removal was found to be superior to the usually applied procedures which include filtering in Fourier space. The reason is that filtering in Fourier space may change the profiles of the absorption lines in such a way that the derived H_4 values (see below) may be systematically offset with respect to the true values. The appropriate order of the polynomial fit was determined from Monte Carlo simulations (see below).

Estimates for the LOSVDs and kinematic parameters were derived from the continuum-removed spectra using the Fourier correlation quotient (FCQ) method (Bender 1990). In this method, the peak of the galaxy template correlation function is deconvolved with the peak of the autocorrelation function of the template star in order to determine the LOSVD. It was shown by Bender (1990) that this method of deconvolving correlation peaks is significantly less sensitive to template mismatching than the direct deconvolution of galaxy and template spectra as employed in the standard Fourier quotient method (e.g. Sargent et al. 1977). The main reason for the better performance of the FCQ method is that it minimizes crosstalk between different parts of the spectrum. This is of considerable importance because template mismatching is the most severe problem in deriving reliable kinematic parameters of elliptical galaxies. Besides using the FCQ method we tried to reduce mismatching further by comparing results obtained with different templates and choosing the template that gave the smallest mismatch (see below for how mismatching can be identified in the results).

Since Fourier deconvolution, which is also essential to the FCQ method, leads to a strong amplification of high-frequency noise, filtering of the data is required before deconvolution. This was done using an optimal Wiener filter which assumed a Gaussian shape for the power spectrum of the signal (i.e., the galaxy template correlation peak) and a power law for the power spectrum of the noise. In this way, well-fitting models of the complete signal+noise power spectra could always be constructed. Because of the Wiener filtering, the derived LOSVDs do therefore not contain information about high-frequency structures. Our Monte Carlo simulations (see below) showed that, if the signal-to-noise ratio per resolution element is larger than about 30 (which is always true for the data discussed here), then the typical size of the velocity resolution element of the LOSVD is only a little larger than the spectral resolution element of the spectra (i.e. σ_I = 40 to 70 km s^{-1} here).

Because we are interested in measuring deviations from Gaussian LOSVDs and especially the Gauss-Hermite amplitudes H_3 and H_4, the Wiener filter has to be constructed in

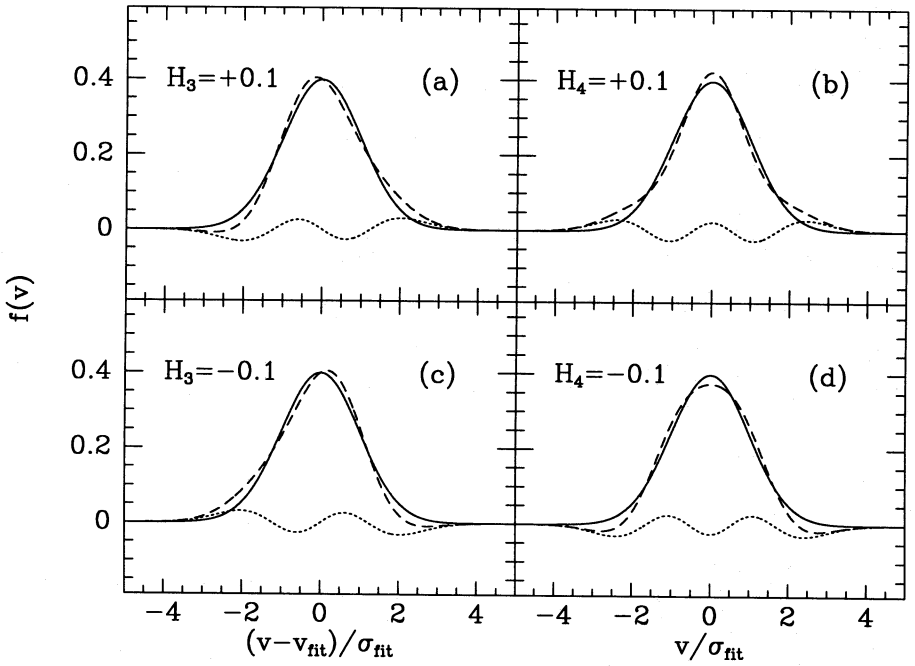

Figure 1. (a) A Gaussian (full line), the third-order Gauss-Hermite basis function of relative amplitude +0.1 (dotted line), and the sum of the two (dashed line, see equation 1). Note how in this case the retrograde wing ($v < v_{\rm fit}$) is *steeper* than the prograde one. (b) A Gaussian (full line), the fourth-order Gauss-Hermite basis function of amplitude +0.1 (dotted line), and the sum of the two (dashed line, see equation 1). Note the triangular shape produced in this case. (c) The same as in (a) but with $H_3 = -0.1$. In this case the prograde wing is steeper than the retrograde one, as observed in elliptical galaxies (see Fig. 4). (d) The same as in (b) but with $H_4 = -0.1$. Note the flat-top shape produced in this case.

such a way that it does not affect the measurement of these parameters. This, however, turns out to be very simple, because the lowest order Gauss-Hermite basis functions contain only little more high-frequency structure than the Gaussian itself. Fig. 2 illustrates this behaviour: it displays the power spectra of the Gaussian and of the third- and fourth-order Gauss-Hermite basis functions of amplitude +0.1 of the Gaussian in Fourier space. It is evident that the latter two extend to only about a factor 1.2 higher frequencies in Fourier space than the Gaussian. Based on these properties, we concluded that, if we chose a factor 1.2 larger width for the Wiener filter than a perfectly adjusted Gaussian would suggest, then the H_3 and H_4 amplitudes would not be affected by the filtering. This was indeed confirmed by Monte Carlo simulations (see below).

Important note. The velocity dispersions σ, as given here, correspond to the parameter $\sigma_{\rm fit}$ of the fit function (equation 1). Only to first order do they equal the second velocity moment of the velocity distribution (differences up to 15 per cent). Similarly, the rotation velocities given also correspond to the fit parameter $v_{\rm fit}$ and again only equal the first moment of the velocity distribution to within 15 per cent. Figs 3(a) and 3(b) show the relation between the true moments and $v_{\rm fit}$ and $\sigma_{\rm fit}$ for a given H_3 and H_4. The skewness and kurtosis are given as well. For the range of H_3 and H_4 values shown here, the moments are still well defined, because $f(v)$ becomes only slightly negative over a limited range in v: see equation (1) (in which case we set $f(v) = 0$ to calculate the moments). Note that the even moments are only weakly dependent on H_3 and that the mean rotation does not depend on H_4 at all.

For the following, we have decided to use the fit parameters $v_{\rm fit}$ and $\sigma_{\rm fit}$, hereafter simply called v and σ, instead

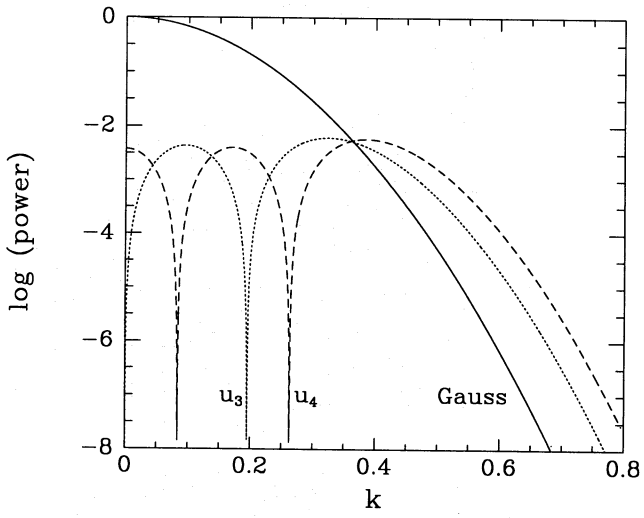

Figure 2. The logarithmic power spectrum of a Gaussian function (full line), of a third-order Gauss-Hermite (dotted line) and of a fourth-order Gauss-Hermite basis function (dashed line) of relative amplitude +0.1. The latter two extend to only about a factor 1.2 higher frequencies in Fourier space than the Gaussian.

of the true first and second moments if velocities or velocity dispersions are needed in the discussion of the results. The reasons for this are (a) the fitted v and σ values more closely correspond to the velocities and velocity dispersions that are derived with the classical methods, (b) correction of velocities and dispersions increases the scatter due to the relatively large errors in H_3 and H_4, and (c) velocities and dispersions would change on average by less than 10 per cent and the conclu-

Table 2. Log of the observations. MJ and MN correspond to major and minor axis respectively. J indicates positions parallel to the major axis, with the number giving the distance from the centre in arcsec. D stands for diagonal axis. The galaxy types were taken from Sandage & Tammann (1987) or derived from our own CCD photometry.

Galaxy	Type	Run #	P.A. (°)	Position	Exp. Time (min)
M81	Sb	6	135	MJ	15
		6	135	J5	15
		6	135	J10	15
		6	135	J15	15
N821	E6	1	30	MJ	60
N1600	E4	4	8	MJ	90
		4	98	MN	113
N1700	E3	5	90	MJ	120
		5	180	MN	120
N2300	E3	5	80	MJ	120
		5	170	MN	120
N2974	E4	1	35	MJ	90
N3115	S0	10	44	MJ	80
		8	44	MJ	90
N3156	E5/S0	6	45	MJ	120
N3193	E2	6	3	MJ	120
N3377	E6	10	42	MJ	60
N3379	E0	9	72	MJ	90
N3607	S0	1	121	MJ	90
N3610	E5/S0	1	135	MJ	90
		4	135	J10	150
		6	135	J5	120
		8	45	MN	135
N3613	E6/S0	1	98	MJ	60
N3640	E2	1	-90	MJ	60
		4	0	MN	90
N3641	E	6	60	MJ	120
N4125	E6/S0	1	82	MJ	60
		6	45	D	67
N4168	E1	6	130	MJ	120
N4278	E1	3	20	MJ	90
N4251	S0	1	103	MJ	88
N4261	E3	1	157	MJ	60
		1	67	MN	60
N4291	E3	4	100	MJ	90
		4	16	MN	75
N4365	E3	1	135	MN	60
		4	42	MJ	90
N4382	S0	1	25	MJ	60
N4406	S0/E3	1	-60	MJ	60
		1	30	MN	80
N4472	E1	6	160	MJ	120
		5	70	MN	135
N4473	E5	2	95	MJ	90
N4486	E0	7	20	MJ	120
N4486B	cE	6	90	MJ	120
		6	0	MN	120
N4494	E1	1	180	MJ	60
N4552	S0	10	119	MJ	45
N4564	E6	1	45	MJ	90
N4589	E2	2	90	MJ	180
N4621	E5	1	163	MJ	90
		8	73	MN	120
N4636	E0/S0	10	149	MJ	50
N4649	S0	5	100	MJ	120
		5	10	MN	120
N4660	E5	1	98	MJ	90
		8	5	MN	85
N5322	E4	1	98	MJ	110
		1	8	MN	90
		7	93	J4	112
N5576	E4	2	90	MJ	45
N5846	S0	3	0	MJ	48
N6411	E	7	70	MJ	120
		7	-20	MN	120
N6703	E	7	70	MJ	90
N7454	E	7	-30	MJ	167
N7785	S0/E5	7	138	MJ	90
		7	48	MN	90

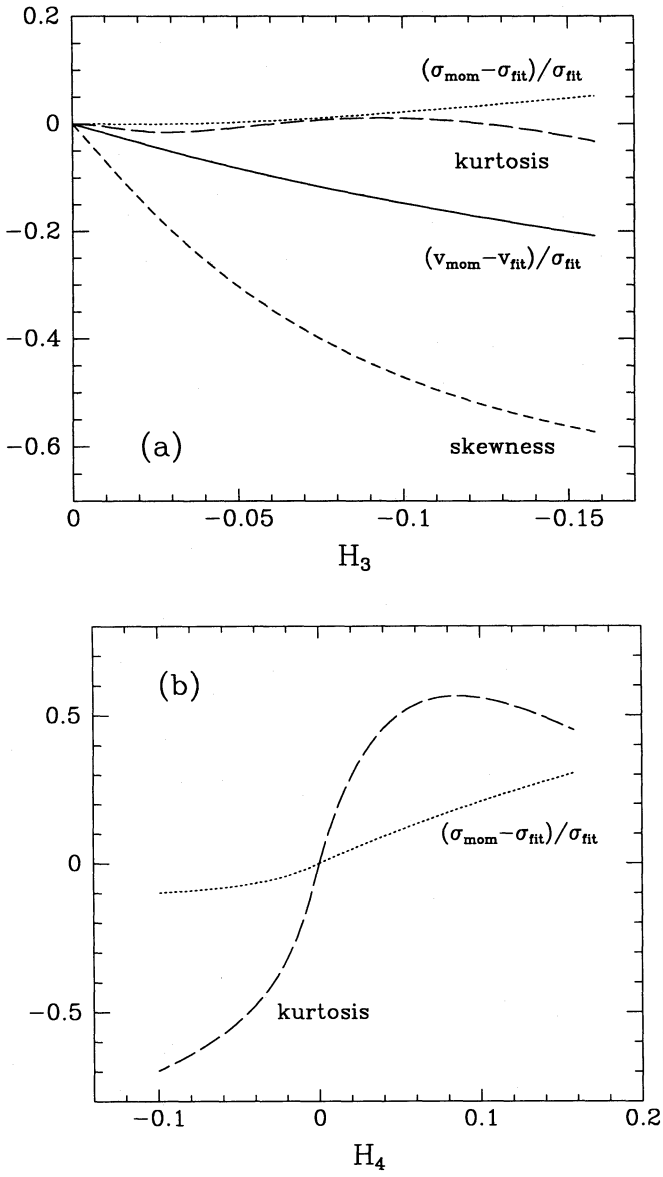

Figure 3. (a) The relation between the true moments and v_{fit} (solid line) and σ_{fit} (dotted line) for a given H_3 and $H_4 = 0$. The skewness (short dashed line) and kurtosis (long dashed line) are given as well. (b) The relation between true moment σ and σ_{fit} (dotted line) and the kurtosis (dashed line) for a given H_4 and $H_3 = 0$.

sions of this paper do not rely on such small differences. For other applications, for example in Jeans' equations, the differences between the fitted v and σ and the true first and second moments may be more important.

Fig. 4 shows the radial profiles of v, σ, H_3, and H_4 for all galaxies observed here. Computer-readable tables are available on request.

3.2 Sources of error and error estimates

The accurate measurement of LOSVDs from absorption line spectra suffers from mainly two problems: template mismatching and inaccurate removal of the stellar continuum. Both effects become more severe with increasing order of the information to be extracted. Averaging of the results obtained

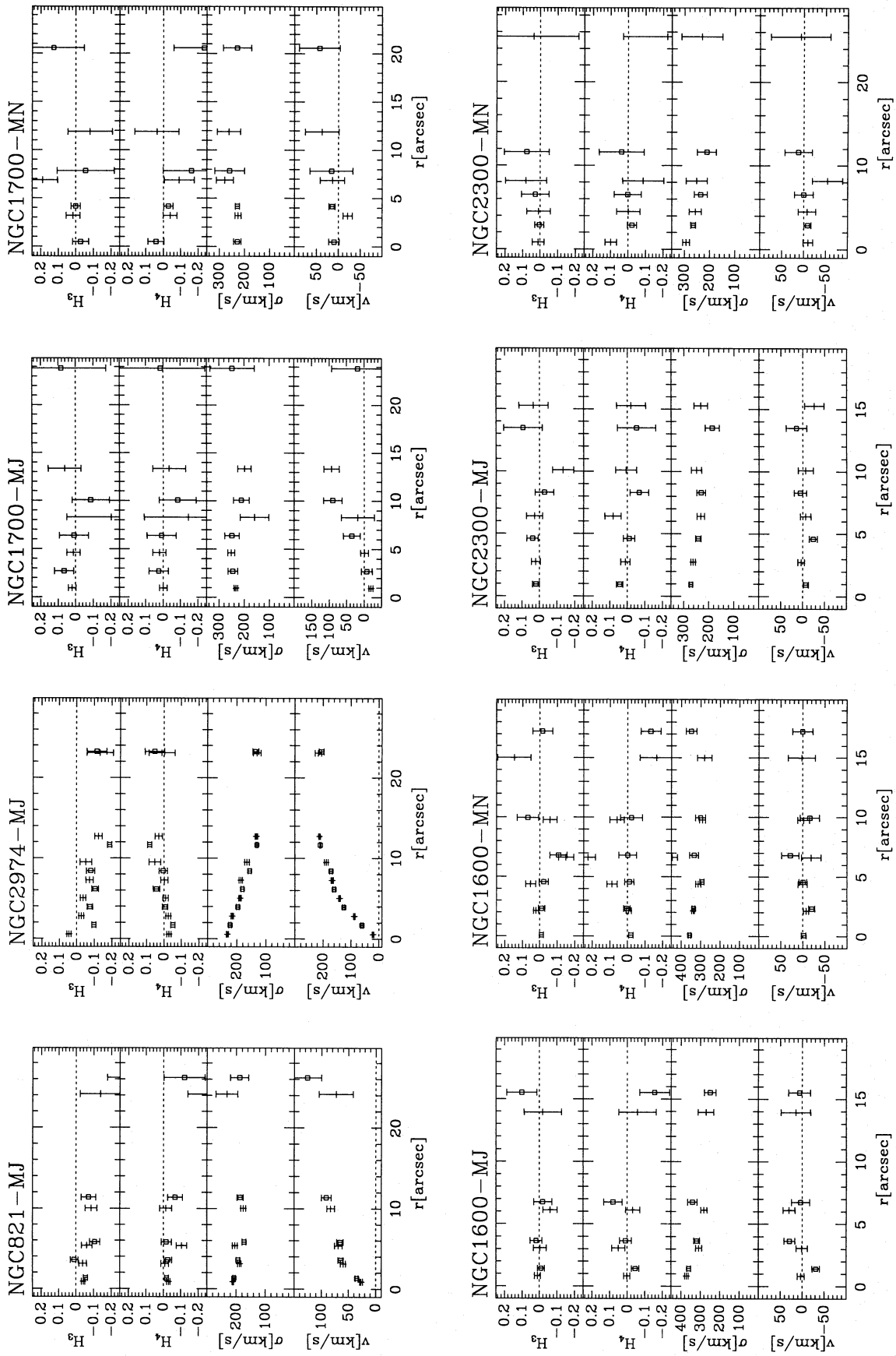

Figure 4. H_3, H_4, σ and v profiles as a function of the distance from the centre for all galaxies of our sample. Crosses and squares refer to opposite sides from the centres of the galaxies. MJ and MN stand for major and minor axis respectively, J indicates a slit position parallel to the major axis, with the number giving the offset in arcsec with respect to the centre. D stands for diagonal axis (see Table 2).

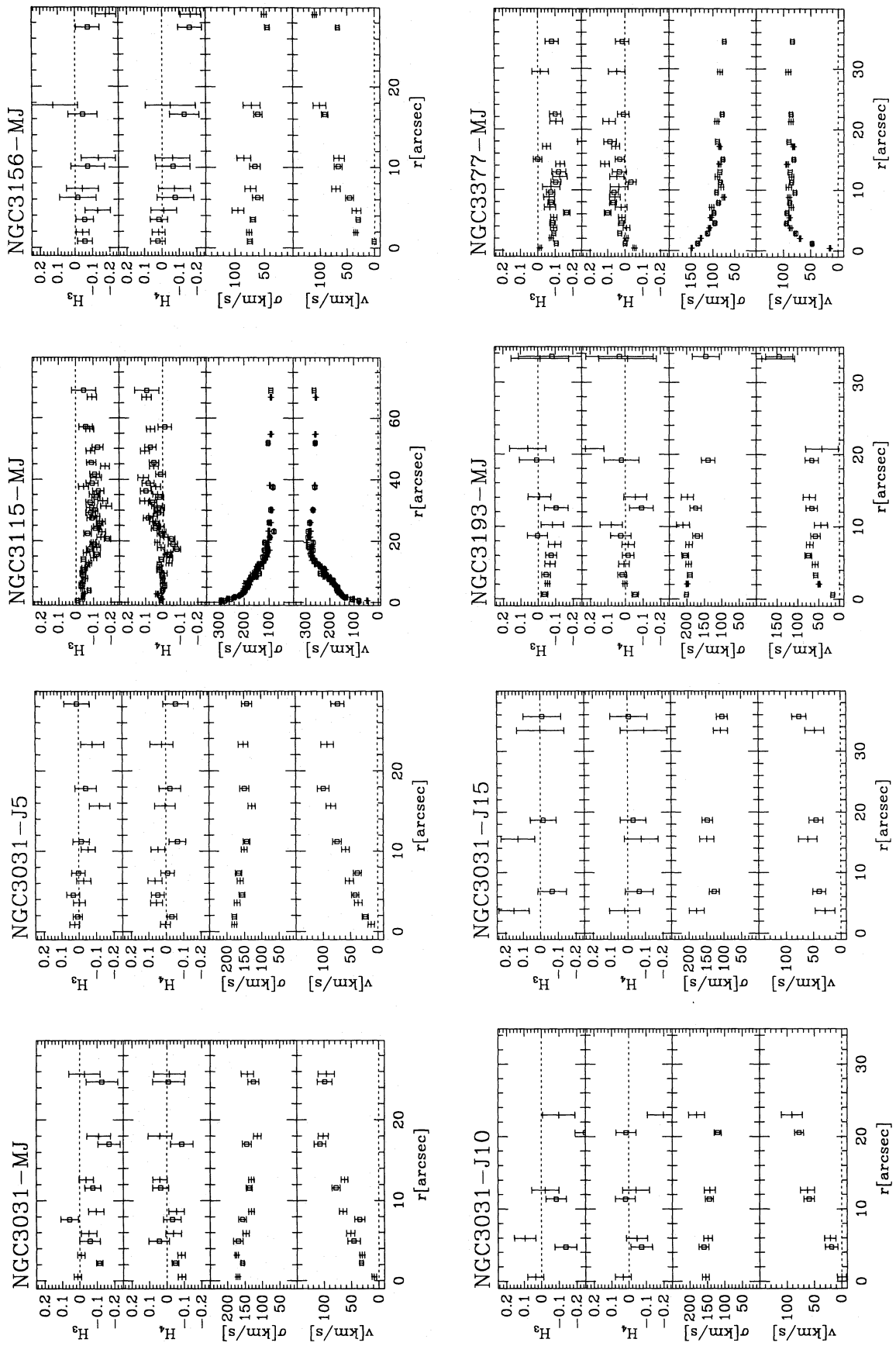

Figure 4 – *continued*

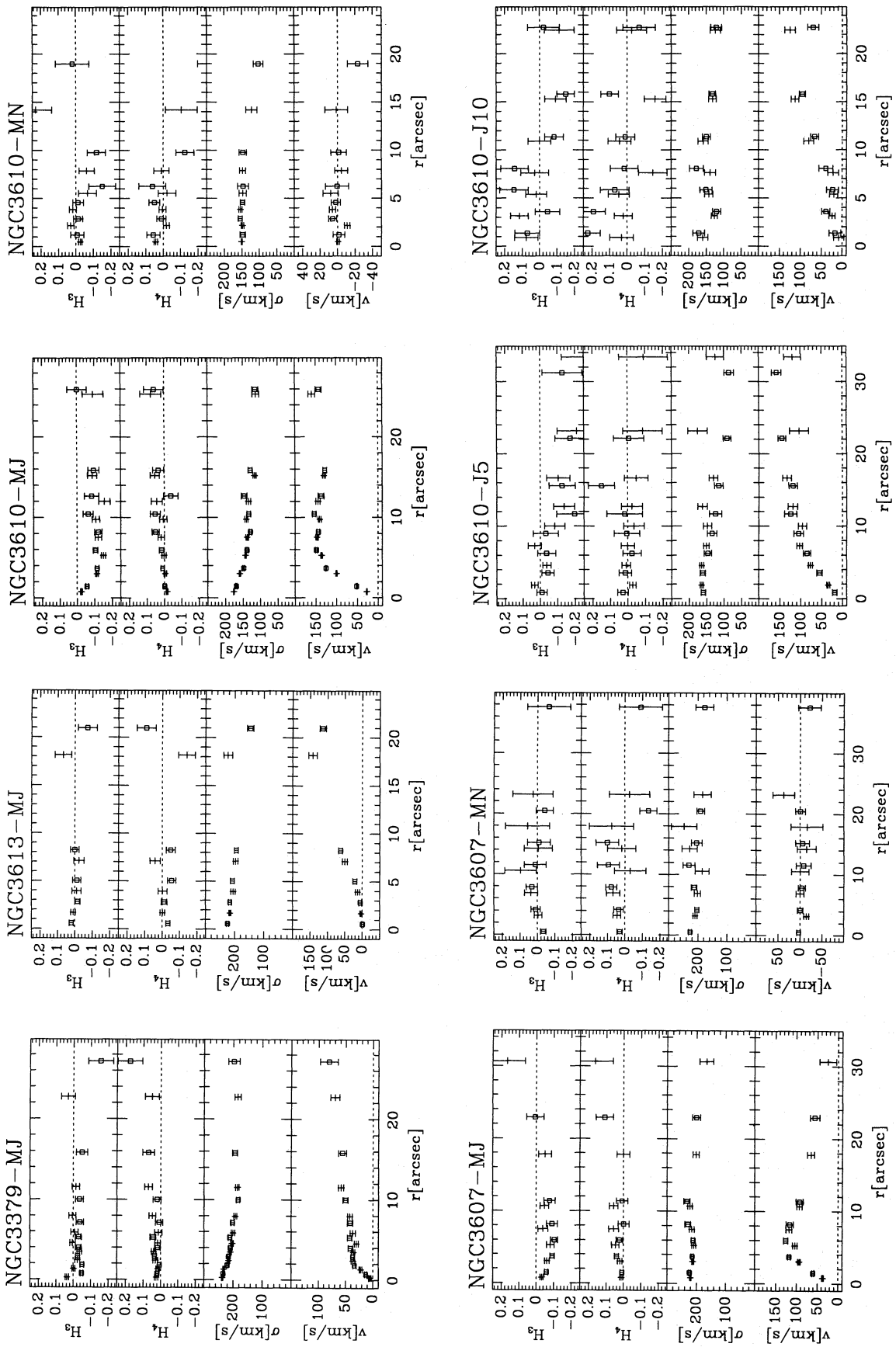

Figure 4 – *continued*

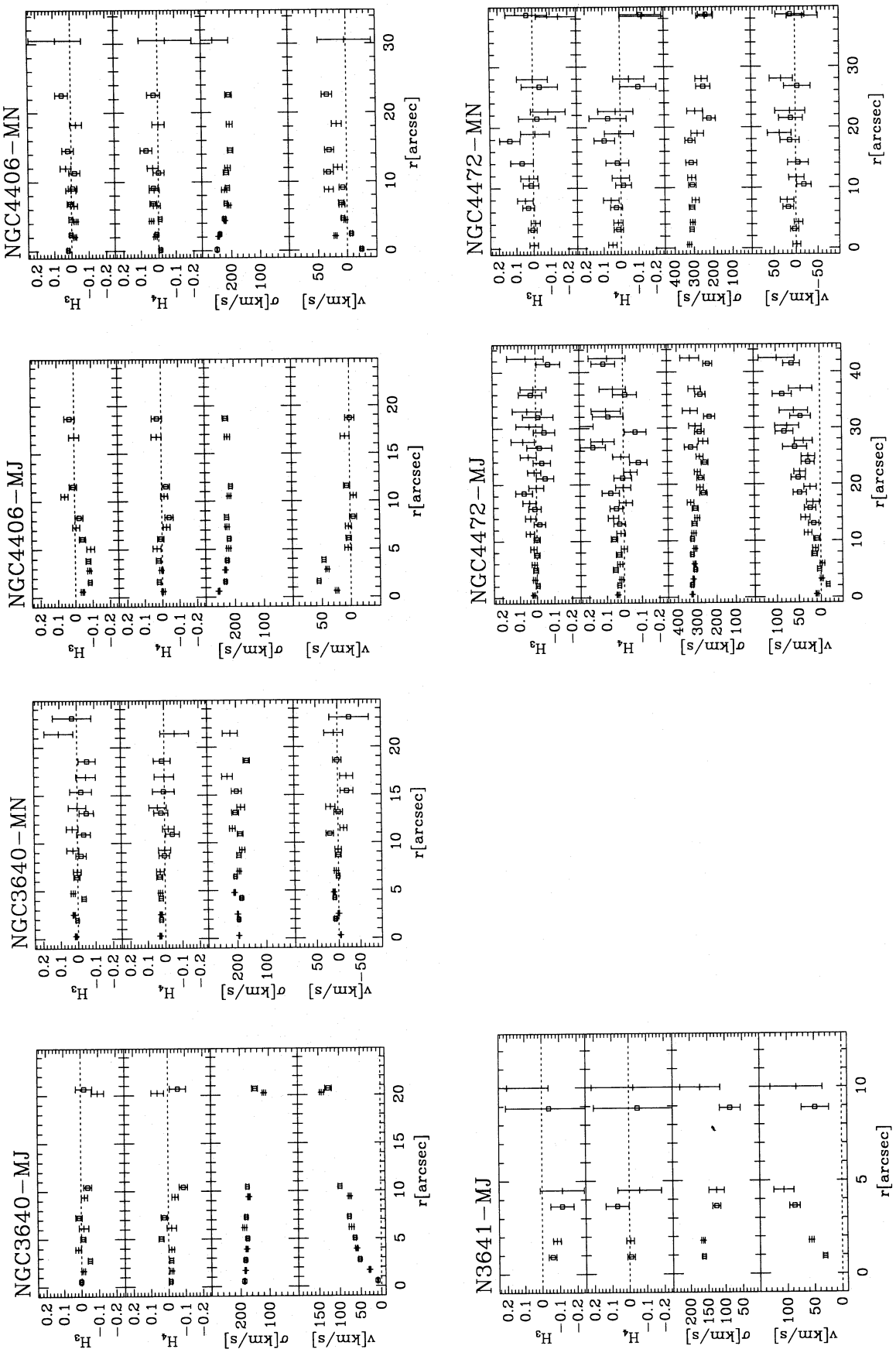

Figure 4 – *continued*

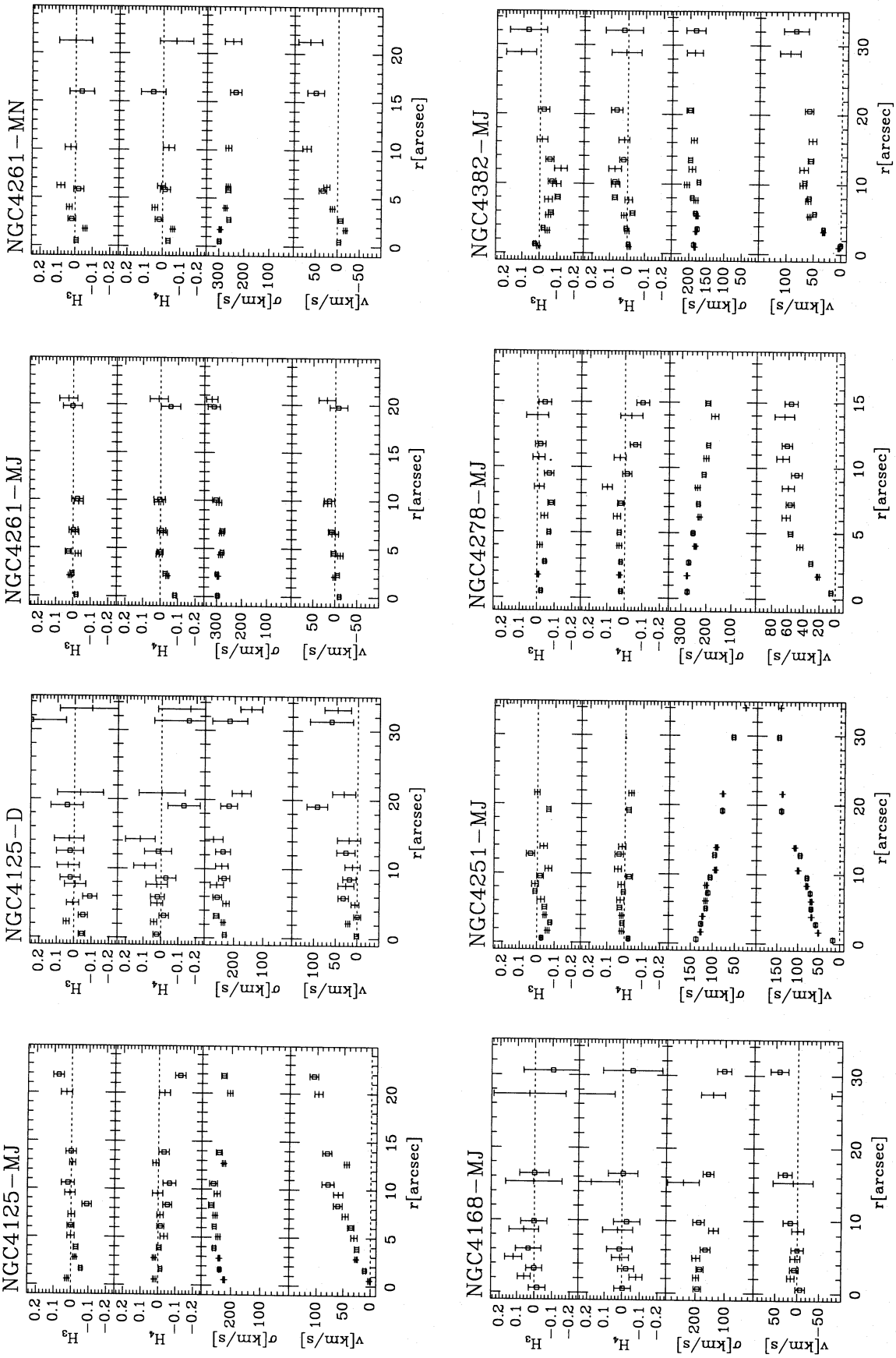

Figure 4 – *continued*

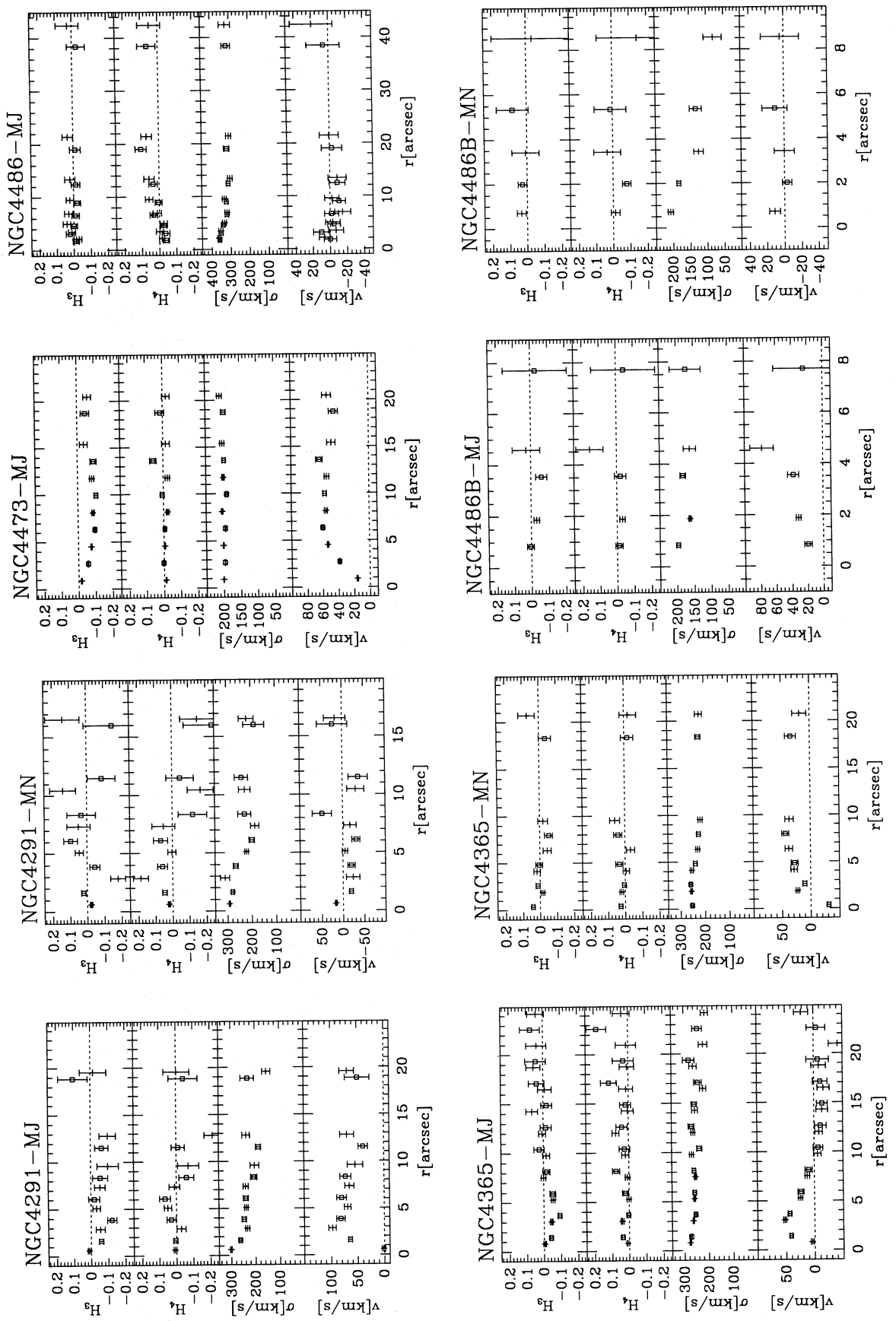

Figure 4 – *continued*

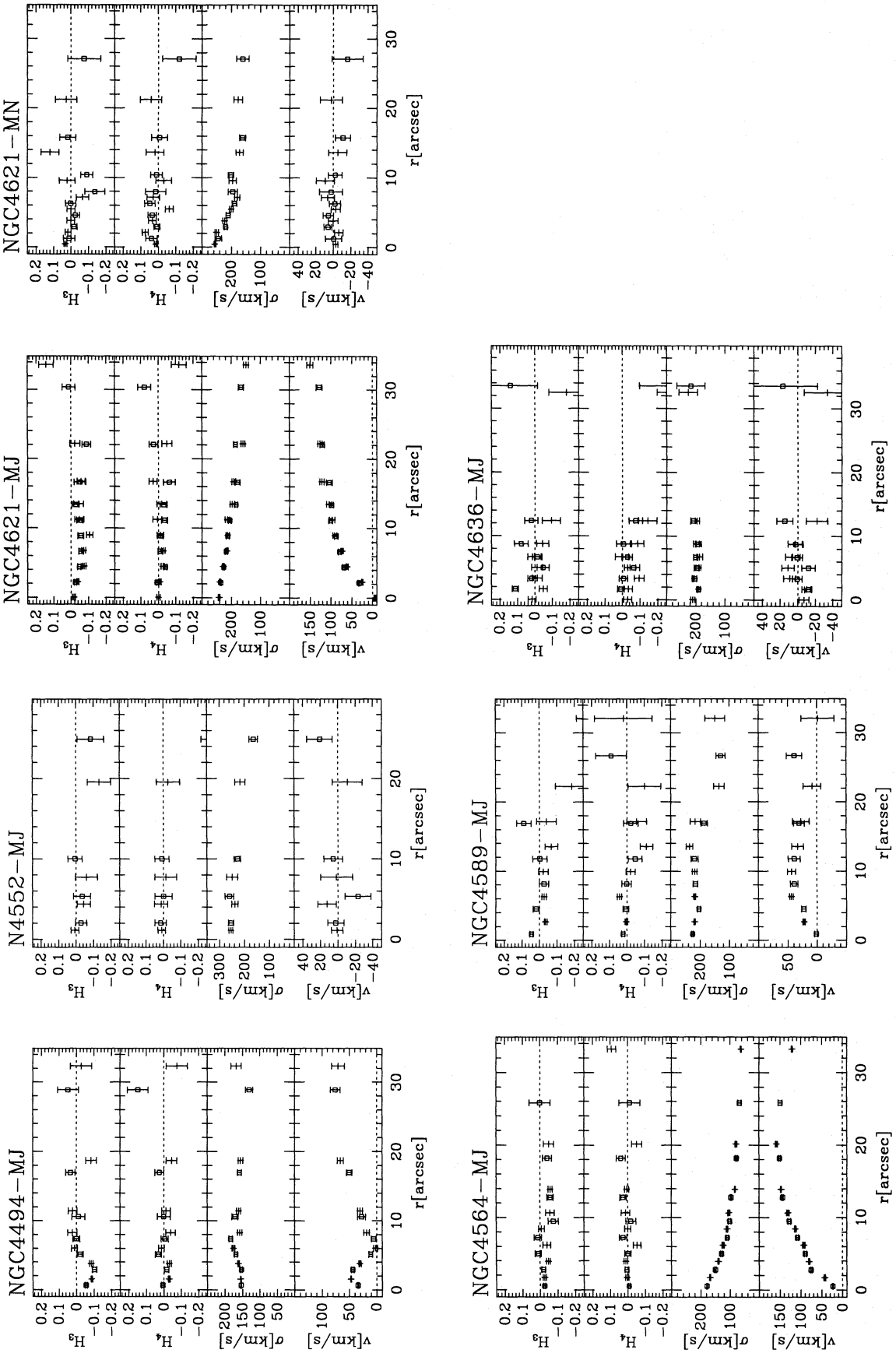

Figure 4 – *continued*

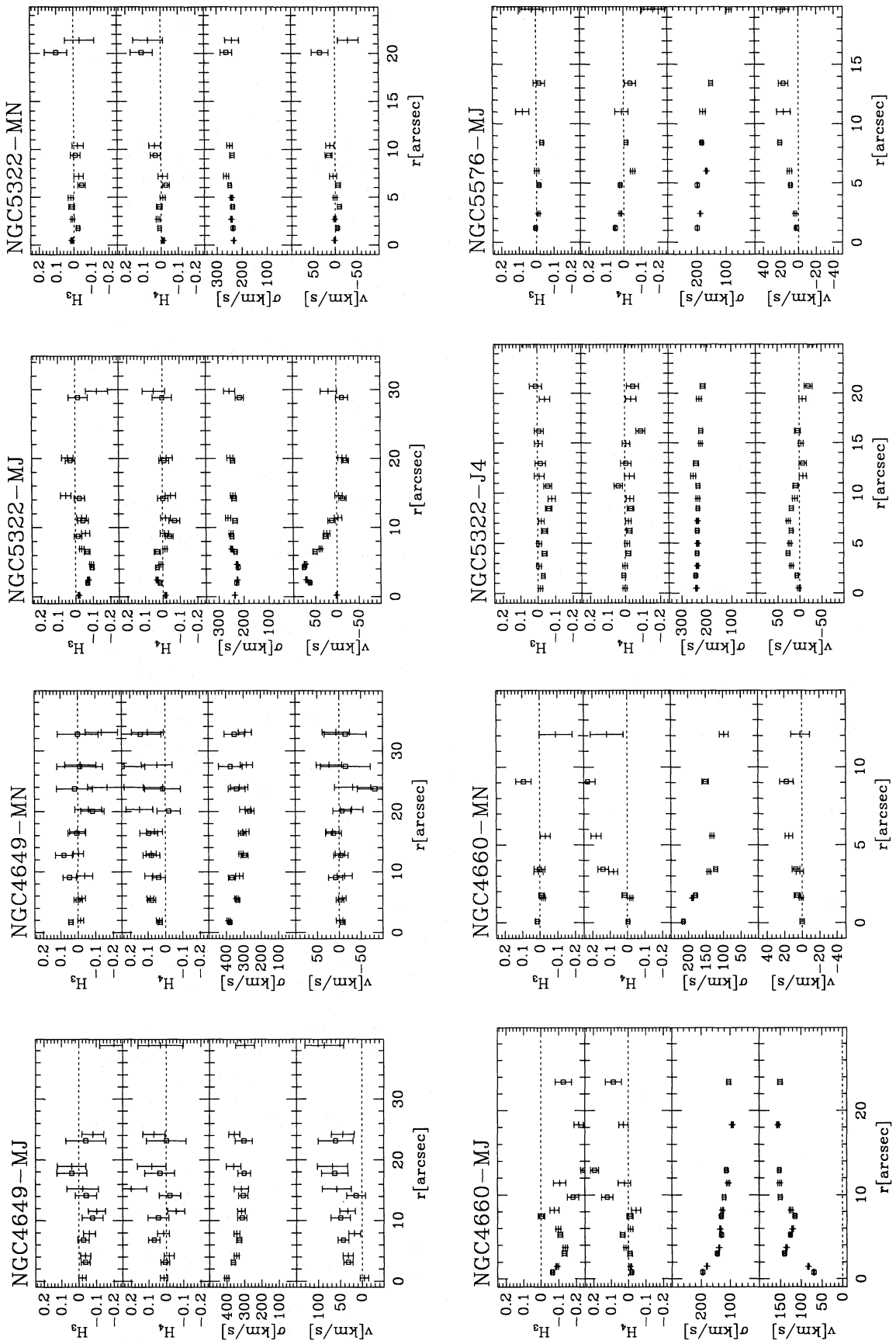

Figure 4 – *continued*

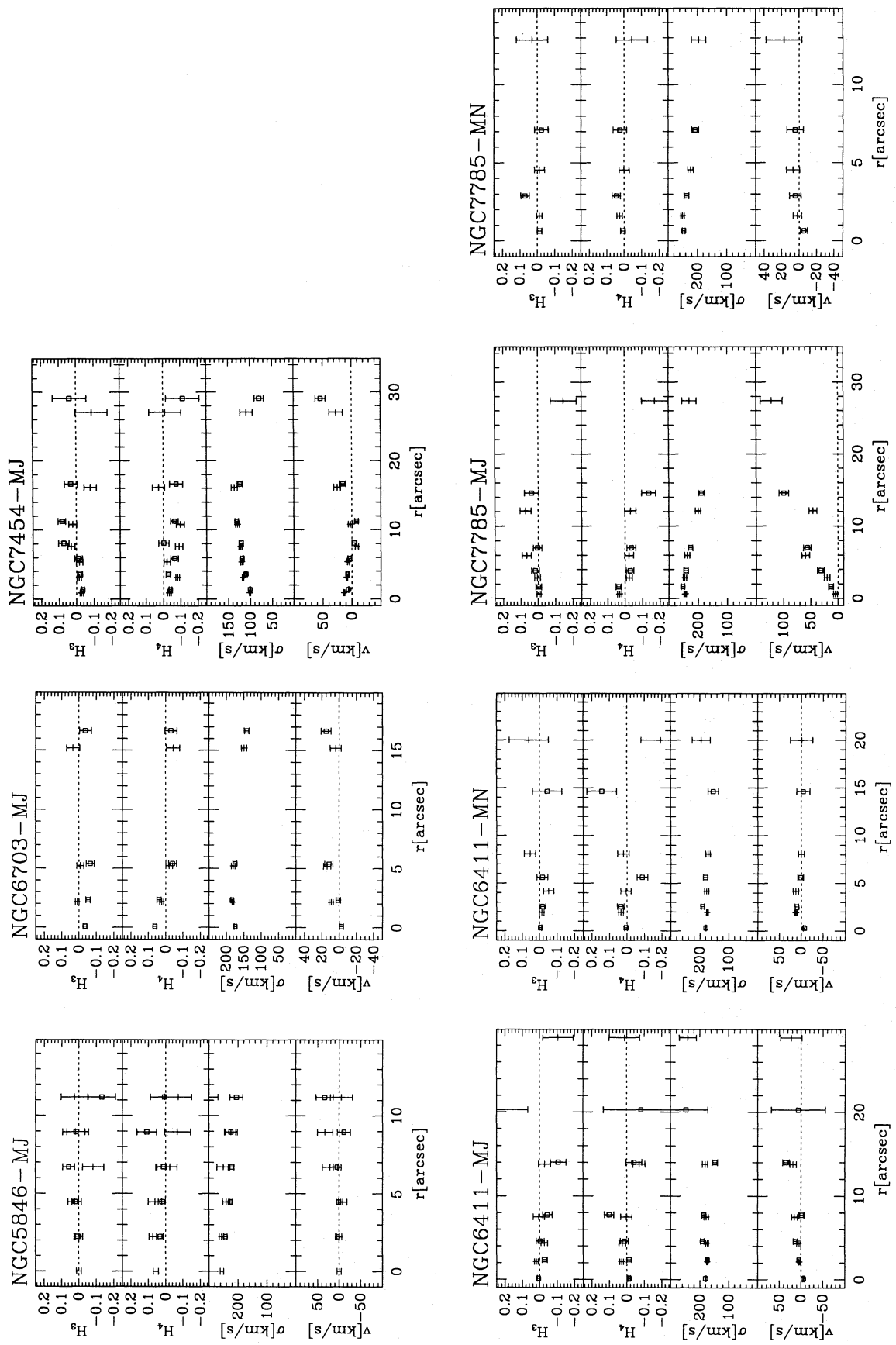

Figure 4 – *continued*

with many different templates or a combination of templates is unfortunately no guarantee that template mismatching is minimized. The fact that the iron peak to light element ratio in ellipticals is systematically different from those of stars in the solar neighbourhood (e.g. Worthey, Faber & Gonzales 1992; Davies, Sadler & Peletier 1993; Carollo, Danziger & Buson 1993) makes template mismatching almost inevitable. Therefore, it is important that one uses a method of deconvolution that minimizes crosstalk between different parts of the spectrum, such as e.g. the FCQ method employed here (Bender 1990) or the method by Rix & White (1992). In addition, selection of templates (or combinations of them) that minimize the symmetric part of the H_3 profile in galaxies helps to minimize mismatching further (for the detailed argument, see below).

Inaccurate sky subtraction is a third but less important problem for the derivation of LOSVDs. Generally, if flatfielding was successful and if the spectrograph slit was sufficiently long that the sky spectrum is not severely contaminated by light from the galaxy itself, then almost perfect sky subtraction can be achieved rather straightforwardly (see e.g. Saglia et al. 1993a). Furthermore, the presence of inaccurate sky subtraction can be easily inferred from kinematic properties that apparently change rapidly at large radii.

In the following, we confine the more detailed discussion of error sources to template mismatching and inaccurate continuum removal. This discussion is based on extensive Monte Carlo simulations which allow us to analyse how the different kinematic parameters depend on these two problems.

(1) Redshifts and, in turn, rotation velocities v are influenced least by both effects.

(2) Velocity dispersions σ are slightly dependent on mismatching, as has been discussed previously by e.g. Kormendy & Illingworth (1982) and Laird & Levison (1985). The dependence of measured velocity dispersions on inaccurate continuum removal can be controlled well, *as long as the velocity distribution is close to a Gaussian.*

(3) The coefficient H_3 is quite insensitive to inaccurate continuum removal but does strongly depend on template mismatching. However, the presence of mismatching can be easily detected. Point-symmetric galaxies should only exhibit completely *asymmetric* H_3 profiles with respect to their centres. Mismatching, on the other hand, will always create a *symmetric* component in the H_3 profile, because it affects the same wing of the broadening function in the same way on both sides of the galaxy. The *symmetric* part of the H_3 profile can therefore be used as a straightforward check for the presence of template mismatching. (The error bars for the *mean* H_3 and H_4 values given in Tables 4 and 5 and the figures include an estimate of the mismatching making use of this fact.)

(4) H_4 is strongly dependent on mismatching and on inaccurate removal of the galaxy continuum. While the influence of mismatching can be roughly estimated from the symmetric part of the H_3 profile (see above), the influence of insufficient continuum removal is difficult to estimate directly (see also van der Marel et al. 1994). Therefore, H_4 is certainly the most uncertain parameter derived here; in particular, the relative errors are large due to the relatively small absolute values of H_4. Only with Monte Carlo simulations can it be shown that for a given observing run (or set-up of the spectrograph and flatfielding) continuum removal is sufficiently accurate to allow a reliable measurement of H_4.

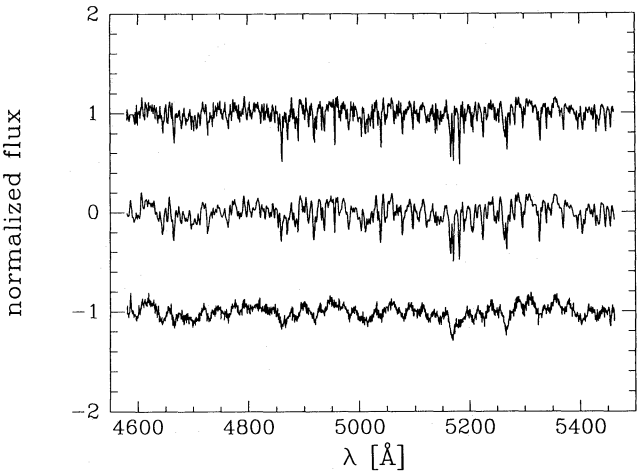

Figure 5. The spectra of a G8III star, a K0III star and a synthetic galaxy created from the K0III star. The test galaxy was broadened to a 'velocity dispersion' of 250 km s^{-1} and noise was added to obtain a signal-to-noise ratio of 33 per pixel (about 50 per resolution element).

As an illustration, Figs 5 and 6 show one set of Monte Carlo simulations that represent a typical case with respect to signal-to-noise ratio and template mismatching. Fig. 5 displays the spectra of a G8III star, a K0III star and a synthetic galaxy created from the K0III star. The test galaxy was broadened to a 'velocity dispersion' of 250 km s^{-1} and noise was added to obtain a signal-to-noise ratio of 33 per pixel (about 50 per spectral resolution element). In addition, there are slight differences in the shapes of the continua. 25 different white noise patterns were tried and the LOSVD of the K0III 'galaxy' was recovered using the FCQ method and the G8III star as a template. Fig. 6 shows the result of these simulations for three types of symmetric LOSVDs, one representing moderately strong radial orbits ($H_4 = 0.10$), one having a small positive H_4 term, and one representing tangential orbits ($H_4 = -0.05$) (cf. the models of Gerhard 1993). The dots represent the 25 recovered LOSVDs, the full line the input LOSVD. It can be easily seen that the template mismatching causes slight asymmetries in the derived profiles and also that the difference in the continua causes the LOSVDs to fall off slightly differently at very large velocities. Nevertheless, the overall shapes of the recovered profiles are quite close to those of the input LOSVDs and, more importantly, the H_3 and H_4 values of input and output do not differ significantly.

With the kind of Monte Carlo simulations just described, it is straightforward to analyse how the rms errors of v, σ, H_3 and H_4 depend on the signal-to-noise ratio of the input spectra and on the shape of the LOSVD. For each observational set-up, the errors in v, σ, H_3 and H_4 as given in this paper were determined from such simulations.

In Fig. 7, we show how the output values and rms errors of H_4 depend on the signal-to-noise ratio of the input spectra, again for three sets of Monte Carlo simulations similar to those shown in Fig. 6. The dotted lines represent the input values of H_4, the full lines the mean H_4 values of 25 different simulations and the dashed lines the 1σ rms curves. These curves are independent of velocity dispersion broadening if the velocity

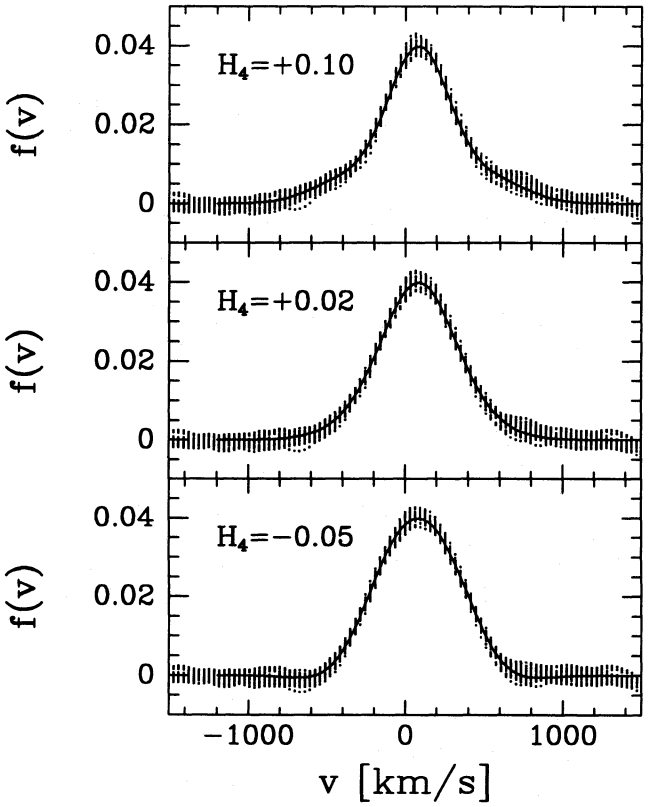

Figure 6. Monte Carlo simulations to recover three different types of LOSVDs (radial, nearly Gaussian, tangential). The K0III 'galaxy' of Fig. 5 with 25 different noise patterns added was analysed using the G8III star of the same figure. The full lines represent the input LOSVD, the dots the recovered LOSVDs. For more details, see text.

dispersion is in the range 100 km s^{-1} to 500 km s^{-1}. From Fig. 7 it is clear that with our observational set-up meaningful constraints on the LOSVDs require a minimum signal-to-noise ratio of about 30 per pixel (50 per resolution element). Above this ratio, systematic effects are negligible. Similar conclusions are derived from Monte Carlo simulations of LOSVDs with non-zero H_3. Furthermore, for the observational set-up *used here* (see Section 2) the following exceedingly simple relation holds:

$$\Delta H_4 \simeq \Delta H_3 \simeq \frac{1}{S/N} \quad (4)$$

where ΔH_4 and ΔH_3 are the rms errors of a single H_4 or H_3 measurement and S/N is the signal-to-noise ratio *per pixel* of the input spectrum. (This simple relation may, of course, not be valid if other wavelength regions and/or wavelength ranges are used. It depends on the number and mean strength of the absorption lines considered.)

3.3 Comparison of results with those of other authors

Rotation velocities v and velocity dispersions σ derived here compare very favourably with previous measurements (e.g. Davies & Illingworth 1983; Davies et al. 1983; Davies & Birkinshaw 1988; Franx, Illingworth & Heckman 1989; Jedrzejewski & Schechter 1989). This shows that the velocities

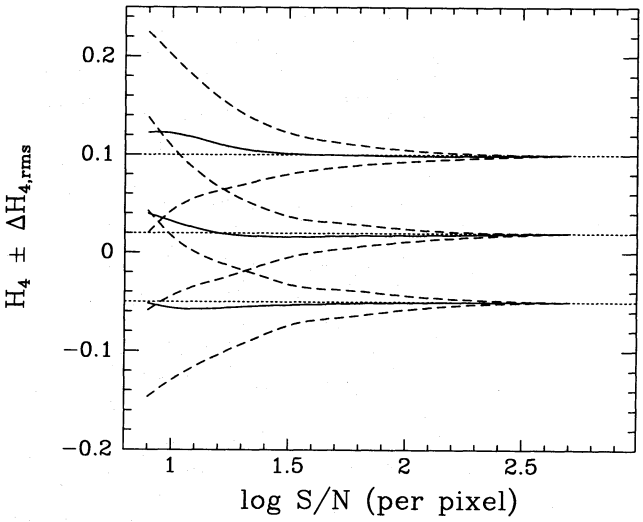

Figure 7. The relation between the signal-to-noise ratio per pixel of the input spectrum and the distributions of output H_4 values. Three different H_4 input values (dotted lines) are given. The full curves show the mean of 25 Monte Carlo experiments, the dashed curves the 1σ boundaries of the H_4 distributions.

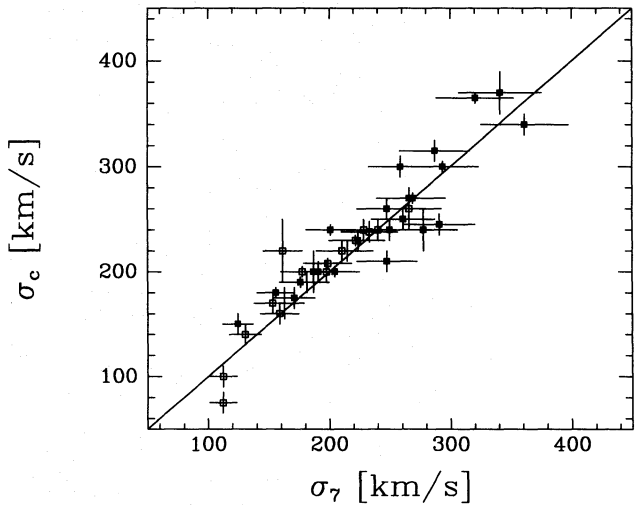

Figure 8. The central values of the velocity dispersions measured here (σ_c) compared with those given by the Seven Samurai (Davies et al. 1987; Faber et al. 1989).

v_{fit}, σ_{fit} obtained here correspond well to the Gaussian fit values of the classical methods for obtaining kinematic data (but neither of these corresponds to the true moments to better than 10-20 per cent for significantly non-Gaussian line profiles).

Fig. 8 compares the central values of the velocity dispersions measured here with those given by Davies et al. (1987) and Faber et al. (1989). The velocity dispersion errors of Davies et al. vary between 9 per cent and 14 per cent; for the sake of simplicity we adopted 10 per cent. We also note that our central velocity dispersions are based on smaller apertures than those of Davies et al., and this is the reason why our values are on average a few per cent higher than theirs.

We also compare (Fig. 9) the rotation and velocity dis-

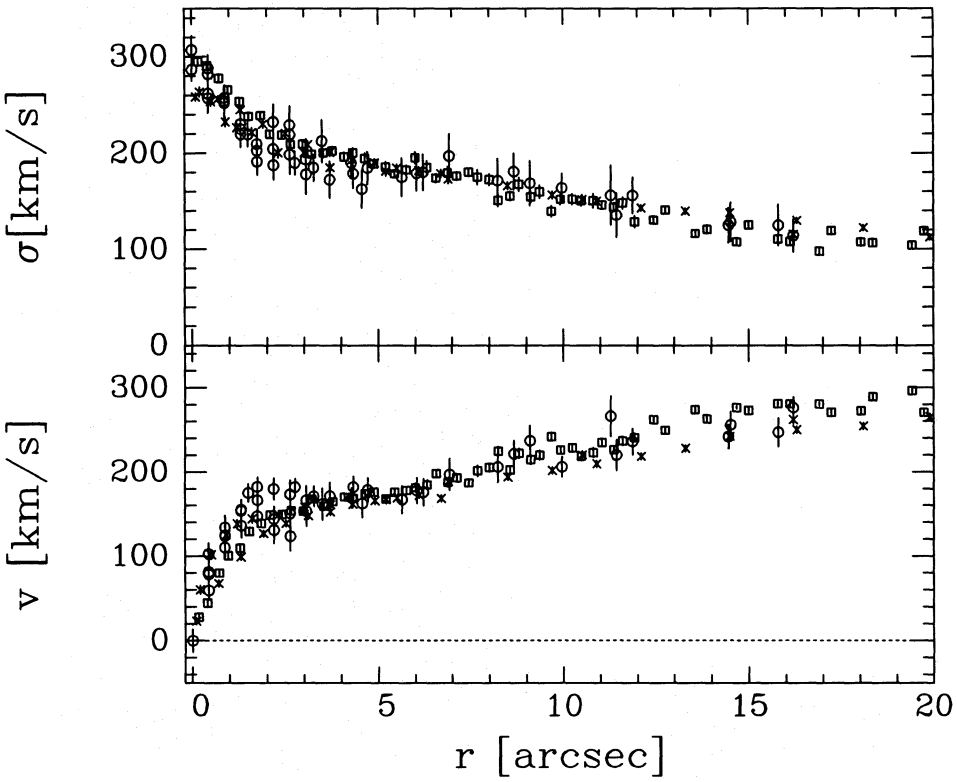

Figure 9. The rotation and velocity dispersion profiles of NGC 3115 along the major axis. Squares represent our measurements, circles the data of Kormendy & Richstone (1992), and crosses the data of van der Marel et al. (1994). The rotation and velocity dispersion curves compare favourably. The residual differences can be fully accounted for by the differences in the observing conditions and set-ups, i.e. they are due to different seeings, slit position angles, and slit widths.

persion profiles of NGC 3115 as derived here with recent measurements of Kormendy & Richstone (1992) and van der Marel et al. (1994). Note that both for Kormendy & Richstone and for van der Marel et al. *two* rotation and velocity dispersion curves are given. These correspond to different seeing conditions. For a comparison of these data with earlier work (especially Illingworth & Schechter 1982), we refer to Kormendy & Richstone (1992). As Fig. 9 shows, the rotation and velocity dispersion curves of the different authors compare quite favourably. The residual discrepancies can be fully explained by the differences in the observing conditions and set-ups, i.e. they are due to different seeing values, slit position angles, and slit widths (which cause different fractions of disc light to fall in the slit).

There are only three galaxies in our sample for which previous measurements of H_3 and H_4 have been obtained. These are NGC 2974, NGC 3115 and NGC 4278 (Cinzano & van der Marel 1993; van der Marel & Franx 1993; van der Marel et al. 1994). In all of these cases reasonable agreement is observed. The object with the most extensive and accurate data is again NGC 3115. Fig. 10 shows the H_3 and H_4 profiles of NGC 3115 along the major axis, as derived from our observations (squares) and from van der Marel et al. (crosses). We compare the innermost 20 arcsec only because the two H_3 profiles published by van der Marel et al. differ considerably outside this radius, making a meaningful comparison impossible.

4 SYSTEMATIC PROPERTIES OF LOSVDs: IDENTIFICATION OF REPRESENTATIVE OBJECT CLASSES

Here we will explore the variety of observed LOSVDs in order to highlight their systematics and to identify representative objects and object classes. General correlations between different kinematic and non-kinematic parameters will be discussed in Section 5.

4.1 M87 (NGC 4486) and other E0 objects

E0 ellipticals are of special interest because there now exists a variety of models that predict LOSVDs for them (Dejonghe 1987; Gerhard 1991, 1993; Merritt 1993), which makes the interpretation of their H_4 profiles more straightforward than in the case of flattened objects even with only little rotation‡. As already mentioned in the introduction, M87 has received much attention in the past because of its presumed central black hole. So far, the evidence from stellar dynamics is still inconclusive (Richstone, Bower & Dressler 1990; see Section 1 for details). Within an ESO key programme, several E0

‡ Some of our nearly E0-type objects show some rotation, and it is likely that these are face-on oblate galaxies in which case their study is more difficult.

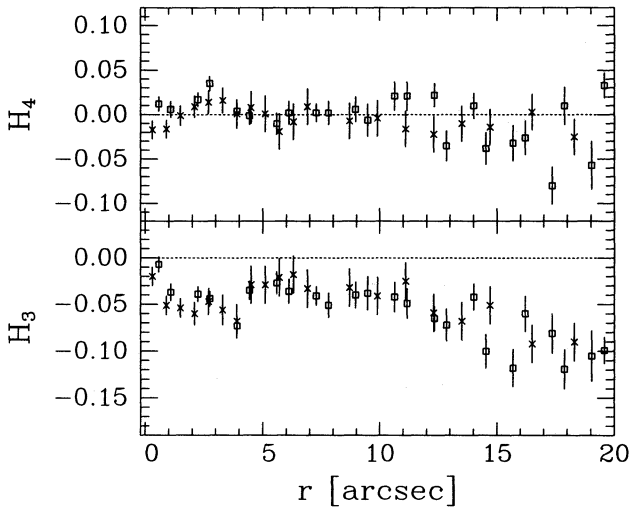

Figure 10. H_3 and H_4 profiles of NGC 3115 along the major axis. Squares represent our measurements, crosses the data of van der Marel et al. (1994).

galaxies have been investigated for the presence of dark haloes (Saglia et al. 1993a; Bertin et al. 1994), but again the results depend on the uncertain velocity anisotropy. The hope now is that the analysis of the LOSVDs in M87 and other spherical galaxies may reduce the degeneracy introduced by velocity dispersion anisotropy, and allow a better determination of their radial mass distributions, both in the nucleus and at large radii.

It is far beyond the scope of this paper to attempt any detailed interpretation of this kind; however, we would like to point out an interesting property of the H_4 profile of M87 and speculate on its implications. The photometric core radius of M87 is about 6 arcsec ($\sim$ 500 pc; Kormendy 1985; Lauer et al. 1992). Inside 6 arcsec the velocity dispersion increases by about 15 per cent (Dressler & Richstone 1990; Fig. 10 above), but, as our analysis now shows, also the H_4 profile changes sign from positive to negative values. Although we have a slight mismatching problem in the analysis of M87 (see the H_3 profile) which may cause our H_4 profile to have a systematic offset, this offset is likely to be constant over the radial range considered here, so we can state that H_4 is smaller inside the core than further out.

To interpret this, note that isotropic spherical models with various central cusps (the γ-models, Dehnen 1993) have positive central H_4 unless the cusp becomes as steep as $\propto r^{-2}$ (which can be ruled out for M87), and have smaller values of H_4 at larger radii – in other words, show a trend opposite to that observed. Oblate isotropic rotator models with the same density cusps and seen face-on preserve this trend; the only difference is that the H_4 profiles are shifted towards more positive values (fig. 12 of Dehnen & Gerhard 1994). Essentially, the greater the intrinsic flattening, the more circular orbits are needed in these models, and these have relatively low velocities when seen face-on. On the other hand, radially anisotropic models, both spherical (Dejonghe 1987; Gerhard 1993) and oblate (Dehnen & Gerhard 1993), may be able to explain the observed trend. In the centre, the radial orbits mainly contribute at large velocities (i.e., add negative H_4; compare Fig. 1), whereas further out they are seen more nearly side-on and contribute at low velocities (add positive H_4). More detailed modelling is required to determine whether a constant mass-to-light ratio radially anisotropic model can be constructed that fits all the photometric and kinematic data for M87.

4.2 NGC 4660 and other discy ellipticals

This object, although always been classified as an elliptical (e.g. Sandage & Tammann 1987), most certainly contains a stellar disc (Bender, Döbereiner & Möllenhoff 1988; Rix & White 1992), which contributes about 30 per cent of the total light of the galaxy (Scorza & Bender 1994). NGC 4660 is prototypical for the class of so-called discy ellipticals which show structural and kinematic properties intermediate between slowly rotating (boxy) ellipticals and S0-galaxies (Bender et al. 1989).

The superposition of a hot (rotating) bulge and a cold, fast rotating disc will naturally cause asymmetric line-of-sight velocity distributions (e.g. Bender 1990; Rix & White 1992) which are characterized by strong negative H_3 values. This is nicely illustrated with the example of NGC 4660, where features in the major axis rotation curve that are caused by varying light contributions of the disc are reflected by similar features in the H_3 profile (see Scorza & Bender 1994 for a detailed discussion). Fig. 11(a) shows the LOSVD of NGC 4660 on the major axis at $r = \pm 3$ arcsec. If the disc is not perfectly edge-on, as is the case with NGC 4660, its presence should also show in the H_4 profile on the minor axis, where the disc rotation velocities project to zero and the cold disc and hot bulge will be superimposed with no relative shift. This will produce an LOSVD that is similar to the sum of two centred Gaussians with very different widths, i.e. with strongly positive H_4 and no significant H_3 values. This is indeed observed along the minor axis of NGC 4660 (Fig. 11b). Thus the LOSVDs of NGC 4660 appear to be consistent with a two-component disc-bulge interpretation. That this is true not only qualitatively but also quantitatively is shown by Scorza & Bender (1994), who construct a complete photometric model of the two-dimensional light distribution of the disc and bulge and show that the superposition of corresponding kinematical components is consistent with the observed major and minor axis H_3 and H_4 profiles.

Other, strongly discy objects in our sample are NGC 821, 2974, 3031 (M81), 3115, 3377, 3610, 4251, 4473, 4564, and 4621. Typically, the largest H_3 values on the major axis are seen at those radii where the respective disc component contributes most to the light. Those objects for which we have also minor axis data show qualitatively similar (albeit weaker) signatures in H_4 to those in NGC 4660.

4.3 NGC 4365 and other ellipticals with decoupled core kinematics

The existence of kinematically decoupled cores in ellipticals has been known since 1988 (Franx & Illingworth 1988; Jedrzejewski & Schechter 1988; Bender 1988a). Quite early, it became clear that these peculiar core properties are likely to be due to flattened, rapidly rotating components, embedded in the otherwise dynamically hot galaxies (Franx & Illingworth 1988; Bender 1990; Rix & White 1992; Surma

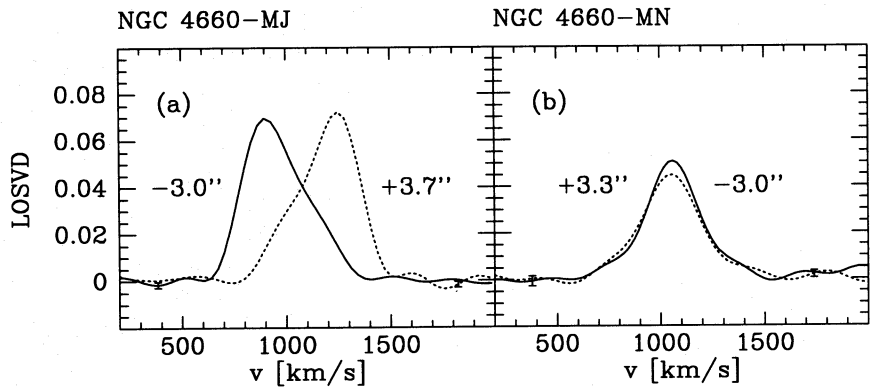

Figure 11. (a) The LOSVD of NGC 4660 along the major axis at a distance of +3 arcsec (dashed line) and −3.0 arcsec (full line) from the centre. Two typical errorbars are shown. (b) The LOSVD of NGC 4660 along the minor axis at +3.3 arcsec (dashed line) and −3.0 arcsec (full line) from the centre.

1992). Furthermore, because of their high metal absorption line-strengths and relatively large masses of up to $10^{10}\,M_\odot$, these components most likely formed from pre-enriched gas that fell to the centre during (possibly early) major merging events (Bender & Surma 1992; Bender, Burstein & Faber 1993).

The principal structure of the decoupled core regions is similar to that of discy ellipticals, with the following two important differences: (a) the radial extents of the phenomena are different, and (b) unlike in discy ellipticals the decoupled cores do not have their angular momentum vectors aligned with those of their bulges. As for discy ellipticals we find significant asymmetries in the LOSVDs of ellipticals with decoupled cores (see, e.g., Fig. 12 for NGC 4365), stemming again from the superposition of a hot slowly rotating and a cold rapidly rotating component; this confirms earlier work by Franx & Illingworth (1988), Bender (1990) and Rix & White (1992). In all objects of our sample with strong rotational features in their core regions (NGC 4365, 4406, 4494, 5322), H_3 has the opposite sign to v, and the reversal in the rotation corresponds approximately to the radius where also H_3 changes sign (see Fig. 4). NGC 1700 and NGC 4472 are also known to have kinematically decoupled cores (Franx et al. 1989; Davies 1988), but we do not detect the same effect there because either the rotation amplitude is too low, as in NGC 4472 (suggesting that the peculiar component does not contribute as much light as in the other galaxies or that it is closer to face-on), or our signal-to-noise ratio and spatial resolution are not good enough to measure a significant H_3, as in NGC 1700.

4.4 Flattened boxy ellipticals without rotation

Objects with these properties are NGC 1600, NGC 2300, NGC 4261 (which shows minor axis rotation), NGC 4406 (main body), and NGC 6411. Without detailed modelling we can rule out that two-integral distribution function models (e.g., as constructed by Binney, Davies & Illingworth 1990 or van der Marel 1991) will fit this type of elliptical galaxy. This is because non-rotating two-integral γ-models predict strongly tangential LOSVDs with $H_4 \simeq -0.08$ ($H_4 \simeq -0.20$) for an E2 (E4) galaxy at $r \approx R_e/2$ on the major axis (Dehnen & Gerhard 1994). Similar results have been obtained by Evans (1993, 1994) for two-integral models with power-law density distributions. The actual observed LOSVD in NGC 4261 is very close to Gaussian ($H_4 \simeq 0$) for $0.1R_e < r < 0.5R_e$. Only in the very centre of NGC 4261 does H_4 become negative; but this may be associated with the central dust lane (Möllenhoff & Bender 1987; Jaffe et al. 1993). The case against two-integral models for the other non-rotating boxy ellipticals is not as strong as for NGC 4261, but nevertheless none of these objects shows an H_4 profile sufficiently negative to be compatible with the predicted negative H_4 values.

Many of the non-rotating galaxies in the present sample have positive values of H_4 on their major axes. How can this be understood? If the indications that ellipticals have near-oblate shapes are confirmed (from analysis of minor axis rotation, Franx et al. 1991; from fundamental plane deviations, Saglia et al. 1993b), then oblate anisotropic models may serve as a first guide. The few such models available with LOSVDs (Dehnen & Gerhard 1993) are not really comparable to the galaxies here because they have isochrone density fall-offs $\propto r^{-4}$ which are much steeper than typically observed around $R_e/2 - R_e$. However, taking the results from these models together with the influence of the potential on the LOSVDs of radially anisotropic spherical models (Gerhard 1993), it appears that positive H_4 on the major axis in non-rotating oblate models will require radial anisotropy, but whether this is sufficient is presently not known.

If non-rotating ellipticals are oblate-triaxial, then the effects of x-tube orbits on the line profiles will not be important, although those of the box orbits may (see de Zeeuw 1985 for the nomenclature of orbits in triaxial potentials, and Hunter & de Zeeuw 1992). Box orbits seen side-on will probably contribute to the LOSVD mostly at small velocities, whereas seen end-on they will contribute at relatively larger velocities. Thus it appears that for a relatively large fraction of solid angle the LOSVDs could be made more peaked by the inclusion of box orbits (such that H_4 increases). If, on the other hand, a prolate-triaxial geometry is correct (as is likely for some galaxies with strong minor axis rotation), then x-tube orbits contribute significantly to the LOSVDs. Because the dominant motion in x-tubes is along the major axis of the potential, one again expects them to contribute at predominantly small

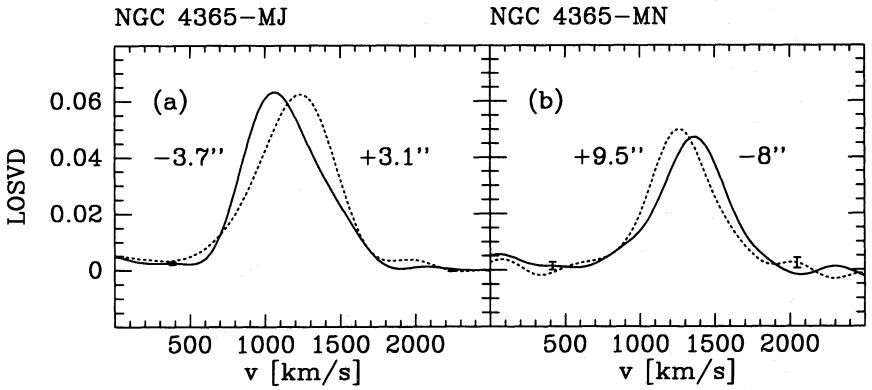

Figure 12. (a) The LOSVD of NGC 4365 along the major axis at +3.1 arcsec (dashed line) and −3.7 arcsec (full line) from the centre. (b) The LOSVD of NGC 4365 along the minor axis at +9.5 arcsec (dashed line) and −8 arcsec (full line) from the centre. Typical errorbars are also shown.

line-of-sight velocities for most viewing directions. But clearly these are speculations before any detailed modelling has been done.

4.5 NGC 4649 and other flattened (boxy) ellipticals with weak rotation

NGC 4649 is supported by anisotropic velocity dispersion but nevertheless shows some rotation along the major axis and also some weak asymmetry in its LOSVD (Fig. 13). The asymmetry is again characterized by negative H_3 values, i.e. it is similar to what we observed for discy ellipticals and ellipticals with decoupled cores, but this time there is no photometric or kinematic evidence for the presence of a colder component. Also the largest measured rotation velocities (near 1 arcsec) in this galaxy do not correspond to negative H_3. This suggests that the asymmetries seen in the LOSVDs of this galaxy are not caused by projection. Other objects falling into this category are, e.g., NGC 4278 and NGC 4291. Because the H_4 values in NGC 4649 are zero or positive, it again appears that two-integral models are not likely to fit this galaxy; but, because of the presence of significant rotation, more detailed modelling is required to confirm this conclusion.

5 CORRELATIONS BETWEEN DIFFERENT KINEMATIC AND NON-KINEMATIC PROPERTIES AND LOSVDs

In order to investigate the correlations between different kinematic and non-kinematic properties and LOSVDs, we have defined mean parameters that describe an individual galaxy sufficiently well. This was done as described below (mostly in accordance with previous publications as far as velocity dispersions and rotations are concerned, e.g. Davies et al. 1983). Note that all mean parameters refer to the galaxy properties *inside* their effective radii.

(1) Characteristic values of *rotation* v *and* $\langle H_3\rangle$, $\langle H_4\rangle$ were obtained from averaging the values of these parameters over most of the observed radial range but excluding the central parts. If possible, only those regions where the rotation curves appeared flat were used. Errors for these mean parameters were estimated on the basis of their radial point-to-point variance. The part of the H_3 profile symmetric with respect to the galaxy centre was used to estimate the amplitude of mismatching in $\langle H_3\rangle$ and $\langle H_4\rangle$; this amplitude was added quadratically to the error estimate from the point-to-point variance. Note that, because in general $H_3 < 0$ (see below) and because we use fit-parameters v and σ instead of true first and second moments, there is a tendency systematically to overestimate the true v/σ by about 10-20 per cent.

(2) *Mean velocity dispersions* σ_m were derived by averaging the velocity dispersions within the isophote corresponding to half the effective radius of each object (effective radii were taken from Burstein et al. 1987 and from own CCD images). *Relative velocity dispersion changes* along the major and minor axes were defined via $\Delta_{\sigma,ma} = (\sigma_{a_e/2,ma} - \sigma_c)/\sigma_c$ and $\Delta_{\sigma,mi} = (\sigma_{b_e/2,mi} - \sigma_c)/\sigma_c$ with a_e and b_e corresponding to the major axis and minor axis lengths of the effective isophote and σ_c being the central velocity dispersion. Due to the generally rather flat velocity dispersion profiles at the effective radii of the galaxies, the $\Delta_{\sigma,ma}$ and $\Delta_{\sigma,mi}$ would not be significantly different if defined on a circle with radius $R = R_e$.

(3) The *anisotropy parameter* $(v/\sigma)^*$ is defined as in Kormendy (1982)§: $(v/\sigma)^* = (v/\sigma_m)/\sqrt{\varepsilon/(1-\varepsilon)}$, where ε is the ellipticity of the galaxy in the same radial range from which v is determined. Galaxies with $(v/\sigma)^* \approx 1$ are supported by rotation, while galaxies with $(v/\sigma)^* < 1$ must have anisotropic velocity dispersions. Ellipticities ε were mainly taken from Bender et al. (1988); for a few objects ellipticities were derived from our own unpublished CCD photometry. The ellipticity values typically correspond to the same radius range from which the characteristic values of v, $\langle H_3\rangle$ and $\langle H_4\rangle$ were derived. Again, due to the fact that we use fit-parameters v and σ instead of true first and second moments, $(v/\sigma)^*$ is systematically overestimated. In any case, the uncertainty in $(v/\sigma)^*$ is large because ε is usually at best determined to within ± 10 per cent.

(4) The amplitude of minor axis rotation can serve as a measure of triaxiality according to Binney (1985). Like him, we will define a *triaxiality parameter* $\mu = v_{min}/\sqrt{v_{min}^2 + v_{maj}^2}$.

(5) Photometric parameters used here are absolute blue magnitude M_B, effective radius R_e, ellipticity ε, major axis position angle $P.A.$ and isophotal shape parameter a_4/a (negative a_4/a describe boxy isophotes, positive a_4/a discy isophotes).

§ This definition is an approximation to the original formula due to Binney (1978).

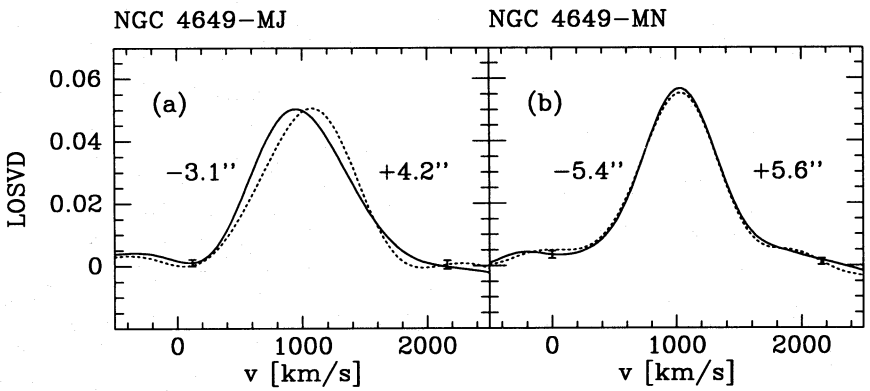

Figure 13. (a) The LOSVD of NGC 4649 along the major axis at +3.1 arcsec (dashed line) and −4.2 arcsec (full line) from the centre. (b) The LOSVD of NGC 4649 along the minor axis at +5.6 arcsec (dashed line) and −5.4 arcsec (full line) from the centre. Typical errorbars are also shown.

These parameters were taken from Burstein et al. (1987) or Bender et al. (1988), or were derived from unpublished CCD photometry, and are listed in Table 3. Where radial averaging had to be done, it was carried out consistently with the averaging of rotation velocities and $\langle H_3\rangle$, $\langle H_4\rangle$ (see above). Distance-dependent quantities were derived using $H_0 = 50$ km s^{-1} Mpc^{-1}.

All characteristic parameters that were derived are listed in Tables 4 and 5. Inspection of the typical $\langle H_3\rangle$ and $\langle H_4\rangle$ values leads to the first general conclusion of our analysis: *LOSVDs in elliptical galaxies are generally close to Gaussians inside the effective radius. However, significant deviations do exist and they amount to typically a few per cent of the peak value of the LOSVD.* This implies that velocities and velocity dispersions that were derived with the classical methods typically do not deviate from the true moments by more than 15 per cent. Whether these deviations correlate with other galaxian parameters will be explored in the following subsections.

5.1 Correlations including $\langle H_3\rangle$ and $\langle H_4\rangle$

We systematically surveyed all parameter combinations for possible correlations with $\langle H_3\rangle$ or $\langle H_4\rangle$. The most interesting correlations (or non-correlations) are described in the following.

The most significant correlations involve $\langle H_3\rangle$ and the isophotal shape parameter a_4/a on the one hand, and $\langle H_3\rangle$ and the anisotropy parameter v/σ_m on the other hand (Fig. 14). As Fig. 14(b) shows, $\langle H_3\rangle$ becomes systematically more negative with increasing v/σ_m. Neglecting the scatter, an approximate relation determined by eye and valid for $v/\sigma_m \leq 1$ is

$$\langle H_3\rangle \approx -0.12\, v/\sigma_m. \quad (5)$$

For $v/\sigma_m > 1$ only one data point and three upper limits are available; this is not enough to decide whether the relation saturates or not. There is no object in our sample that shows significantly positive $\langle H_3\rangle$ values at more than the 1σ level. This means that, *if rotation is present, the prograde wing of the LOSVD is always steeper than the retrograde wing*, i.e. all LOSVDs are qualitatively similar to the ones shown in Section 4. This confirms theoretical expectations (e.g., Dehnen & Gerhard 1993, 1994; Evans 1993, 1994) – quite implausible distribution functions are needed to obtain $H_3 > 0$.

It is important to note that not only discy ellipticals (for which we expect negative H_3 simply because of the superposition of two components, see below) show a relation between $\langle H_3\rangle$ and v/σ_m; boxy ellipticals alone appear to conform with this general trend. Because integration of a locally symmetric velocity distribution along the line of sight cannot account for the observed amplitudes of H_3 if $v/\sigma < 2$ (Bender 1990), we can conclude that *the velocity distributions of rotating boxy ellipticals must be intrinsically asymmetric.*

In order to test the influence of a disc on an LOSVD, we did the following simple experiment: we constructed a set of LOSVDs for the spheroid with a plausible variety of H_3 and v/σ_m values and added disc LOSVDs of different intensities. For the disc LOSVD we adopted a Gaussian with $\sigma_{disc} \approx 50$ km s^{-1} and $v_{disc} \approx \sqrt{2}\sigma_{spheroid}$. It turned out that, more or less independently of the H_3 and v/σ_m of the spheroid, addition of discs of varying intensities always moved the object in roughly the same direction, which is indicated by the arrow in the $\langle H_3\rangle - v/\sigma_m$ diagram (Fig. 14b). The arrow has a steeper slope than the fitting line of boxy Es. However, even by adding about 50 per cent disc to a spheroid that was originally close to the mean $\langle H_3\rangle - v/\sigma_m$ relation, it will not be possible to move the spheroid much below this relation. This experiment suggests a simple explanation why discy Es and boxy Es roughly follow the same relationship between v/σ_m and $\langle H_3\rangle$, provided the $\langle H_3\rangle - v/\sigma_m$ relation of the spheroids alone is close to that of boxy Es.

In the context of the global $\langle H_3\rangle - v/\sigma_m$ relation, it is interesting to check whether a similar correlation also exists locally within the galaxies. Fig. 15 shows all local $v/\sigma - H_3$ data points, i.e., all galaxies were plotted on top of each other; only H_3 values with errorbars smaller than 0.05 were included. The distribution is consistent with the findings of van der Marel et al. (1994). For small v/σ the local relation between v/σ and H_3 is steeper than the global relation discussed above, while for large v/σ it is somewhat flatter than the global relation. The former result presumably says that even a small fraction of rotating stars may cause significant asymmetry

Table 3. Photometric parameters and central and isophotal ($R_e/2$) major and minor axis values of the stellar velocity dispersions of the galaxies listed in Table 2. For the origin of the photometric parameters, see text.

Galaxy	R_e ($''$)	M_B	ΔPA (°)	ϵ	$a_4/a * 100$	$\delta a_4/a * 100$	σ_c $\left(\frac{km}{s}\right)$	$\delta\sigma_c$ $\left(\frac{km}{s}\right)$	σ_{maj} $\left(\frac{km}{s}\right)$	$\delta\sigma_{maj}$ $\left(\frac{km}{s}\right)$	σ_{min} $\left(\frac{km}{s}\right)$	$\delta\sigma_{min}$ $\left(\frac{km}{s}\right)$
NGC 821	45.41	-21.31	0	0.36	2.5	0.2	208	5	200	20	–	0
NGC 1600	47.55	-23.17	5	0.35	-1.2	0.2	365	5	250(1)	20	300	20
NGC 1700	13.71	-22.28	2	0.25	0.9	0.2	238	10	200	15	250	20
NGC 2300	36.07	-21.56	7	0.21	-0.6	0.2	270	5	210	20	210	20
NGC 2974	36.91	-21.24	5	0.35	0.5	0.2	230	5	135	10	–	0
NGC 3031	52	-	5	0.30	0.5	0.2	170	10	140	10	–	0
NGC 3115	36.07	-19.96	2	0.65	> 3.5	0.0	260	20	95	5	–	0
NGC 3156	49.79	-19.77	3	0.50	2	0.2	75	10	45	10	–	0
NGC 3193	23.83	-20.08	5	0.12	0.23	0.2	200	5	180	10	–	0
NGC 3377	33.66	-19.49	0	0.48	1.2	0.2	140	10	85	10	–	0
NGC 3379	35.25	-20.17	5	0.09	0.1	0.2	240	5	180	10	–	0
NGC 3607	65.63	-21.02	2	0.20	-0.2	0.2	210	10	160	20	180	20
NGC 3610	12.8	-21.23	0	0.39	2.5	0.2	160	10	130	10	150	10
NGC 3613	24.38	-21.1	0	0.49	0.7	0.2	220	10	200	20	–	0
NGC 3640	32.89	-20.92	8	0.21	-0.2	0.2	190	5	150	10	195	10
NGC 3641	12.22	-18.27	-	0.15	-	0.2	170	15	110	20	–	0
NGC 4125	59.86	-22.33	0	0.42	0.9	0.2	240	10	210	30	–	0
NGC 4168	45.41	-21.25	4	0.14	-	0.2	190	10	140	20	–	0
NGC 4251	15.6	-19.82	2	0.50	> 3.5	0.0	135	5	90	10	–	0
NGC 4261	38.65	-21.74	2	0.22	-1.3	0.2	300	5	310	15	240	20
NGC 4278	32.89	-19.79	15	0.13	0.05	0.2	270	10	180	10	–	0
NGC 4291	14.69	-20.4	2	0.25	-0.3	0.2	300	10	200	10	200	20
NGC 4365	57.16	-20.88	5	0.24	-1.1	0.2	260	10	230	20	220	20
NGC 4382	60	-21.48	2	0.20	0.6	0.2	180	10	180	20	–	0
NGC 4406	90.6	-21.71	5	0.22	-0.7	0.2	240	10	220(2)	20	200	30
NGC 4472	104	-22.21	5	0.17	-0.2	0.2	315	10	270(3)	20	230	30
NGC 4473	24.95	-20.38	0	0.41	0.9	0.2	200	5	200	10	–	0
NGC 4486B	3.07	-17.35	10	0.12	0.8	0.2	220	30	170	20	180	30
NGC 4486	104	-22.06	20	0.05	0	0.2	340	10	320	30	–	0
NGC 4494	45.41	-21.06	9	0.16	0.2	0.2	150	10	150	10	–	0
NGC 4552	30	-20.74	35	0.05	-0.1	0.2	250	10	220	20	–	0
NGC 4564	21.73	-19.61	2	0.55	2.2	0.2	170	10	80	10	–	0
NGC 4589	41.41	-21.22	10	0.19	-	0.2	220	10	150	20	–	0
NGC 4621	46.46	-20.93	0	0.34	1.5	0.2	240	10	160	10	180	10
NGC 4636	101.7	-21.29	10	0.15	-0.1	0.2	200	10	200	30	–	0
NGC 4649	73.64	-21.81	6	0.17	-0.5	0.2	370	20	300	30	330	20
NGC 4660	12.8	-19.39	5	0.45	2.5	0.2	200	10	120	10	130	10
NGC 5322	35.25	-22.03	2	0.31	-0.8	0.2	230	10	240	10	240	20
NGC 5576	19.37	-20.66	0	0.30	-0.5	0.2	200	20	170	20	–	0
NGC 5846	82.63	-21.85	40	0.05	0	0.2	240	20	–	0	–	0
NGC 6411	26.74	-21.78	20	0.30	0	0.2	180	5	180	20	170	20
NGC 6703	23.83	-21.59	20	0.03	0	0.2	175	10	150	20	–	0
NGC 7454	24.38	-20.79	5	0.10	0.5	0.2	100	10	130	20	–	0
NGC 7785	26.74	-22.22	5	0.40	-1.2	0.2	245	10	200	30	200	30

1) From Jedrzejewski & Schechter (1989)
2) From Fried & Illingworth (1994)
3) From Saglia et al. (1993a)

without introducing much rotation; but, since the v/σ values in the central parts of the galaxies tend to be lower than their mean v/σ_m, also seeing may additionally steepen the relation. Fig. 15 also shows the $H_3 - v/\sigma$ relations for two-integral models of different flattening and inclination (Dehnen & Gerhard 1994). The model lines are almost degenerate, showing that even for two-integral models the H_3 versus v/σ relation does not allow us to separate objects of different flattening and inclination. Moreover, it is evident that *non-discy* (= mostly slowly rotating) objects cannot be fitted by two-integral models: the H_3 amplitudes predicted by these models are generally too small. Similarly, discy objects show *larger* H_3 values on average than predicted by two-integral models with spheroidal isodensities. This is further evidence that the discy isophotes in these objects are indeed caused by discs.

Despite the well-defined relationship between H_3 and v/σ_m for all kinds of ellipticals, significant scatter about the mean global $\langle H_3\rangle - v/\sigma_m$ relation clearly exists. This scatter may be partly due to discs or different anisotropies. It is beyond the

Table 4. Mean velocity, velocity dispersion, H_3, H_4 along the major axes of the galaxies listed in Table 2.

Galaxy	v $\left(\frac{\text{km}}{\text{s}}\right)$	δv $\left(\frac{\text{km}}{\text{s}}\right)$	σ_m $\left(\frac{\text{km}}{\text{s}}\right)$	$\delta\sigma_m$ $\left(\frac{\text{km}}{\text{s}}\right)$	$\langle H_3\rangle$	$\delta\langle H_3\rangle$	$\langle H_4\rangle$	$\delta\langle H_4\rangle$
NGC 821	84.4	9.1	195.6	5.7	-0.106	0.030	-0.047	0.041
NGC 1600	7.1	6.8	311.5	15.4	0.003	0.019	-0.018	0.027
NGC 1700	59.3	19.0	244.4	4.2	-0.024	0.059	-0.034	0.035
NGC 2300	5.9	5.0	238.1	9.1	0.020	0.027	0.000	0.022
NGC 2974	191.4	8.0	182.8	10.2	-0.109	0.026	0.034	0.024
NGC 3031	90.5	6.9	146.7	5.1	-0.091	0.038	0.001	0.037
NGC 3115	275.4	2.4	162.4	6.5	-0.110	0.017	0.050	0.019
NGC 3156	77.6	7.6	69.0	4.0	<-0.053	0.00	-0.096	0.024
NGC 3193	80.4	13.4	193.7	4.5	-0.040	0.016	0.020	0.025
NGC 3377	87.5	1.0	97.1	4.1	<-0.093	0.00	0.048	0.013
NGC 3379	50.8	4.9	208.9	4.1	-0.029	0.028	0.041	0.028
NGC 3607	107.7	4.7	211.8	4.7	-0.074	0.018	0.032	0.018
NGC 3610	141.0	2.6	149.8	5.8	-0.109	0.018	0.024	0.018
NGC 3613	92.0	21.6	208.6	4.1	-0.006	0.034	-0.015	0.054
NGC 3640	98.8	12.0	179.7	1.9	-0.029	0.020	-0.020	0.025
NGC 3641	82.9	14.6	144.0	11.0	-0.105	0.017	0.002	0.039
NGC 4125	75.6	8.3	232.0	8.9	0.006	0.019	-0.042	0.018
NGC 4168	10.7	5.4	184.7	9.8	0.021	0.018	0.037	0.039
NGC 4251	124.8	8.5	117.3	3.8	<-0.022	0.00	0.021	0.053
NGC 4261	3.6	3.4	294.5	4.1	-0.001	0.008	-0.012	0.009
NGC 4278	59.6	1.7	229.6	9.5	-0.036	0.022	0.010	0.029
NGC 4291	68.0	4.9	246.0	9.6	-0.046	0.018	-0.025	0.023
NGC 4365	10.0	4.0	260.5	5.9	-0.030	0.011	0.048	0.017
NGC 4382	59.9	2.2	186.7	2.2	-0.063	0.011	0.039	0.012
NGC 4406	1.3	1.9	258.5	27.6	0.003	0.020	-0.007	0.018
NGC 4472	45.4	5.2	294.4	5.2	0.013	0.024	0.050	0.028
NGC 4473	54.4	1.8	198.4	1.4	-0.075	0.012	-0.002	0.013
NGC 4486B	43.2	11.9	179.9	10.0	-0.022	0.025	0.017	0.050
NGC 4486	2.4	2.6	330.0	4.7	-0.009	0.022	0.036	0.023
NGC 4494	53.6	8.5	162.8	2.8	-0.003	0.031	0.007	0.040
NGC 4552	1.3	4.8	247.5	4.8	-0.030	0.017	-0.006	0.037
NGC 4564	143.5	4.8	124.4	8.6	<-0.055	0.0	0.003	0.014
NGC 4589	34.9	2.7	208.1	8.2	-0.009	0.030	-0.025	0.030
NGC 4621	100.7	4.8	208.8	5.5	-0.056	0.0080	-0.016	0.009
NGC 4636	1.7	3.9	201.9	2.7	0.005	0.045	-0.050	0.047
NGC 4649	42.9	5.1	336.8	8.6	-0.037	0.015	0.036	0.021
NGC 4660	138.2	4.5	147.5	9.0	-0.130	0.0200	0.040	0.021
NGC 5322	7.3	5.5	238.7	2.9	0.006	0.028	-0.006	0.015
NGC 5576	10.7	3.0	186.5	5.1	0.006	0.016	0.007	0.015
NGC 5846	6.3	4.8	240.5	7.7	-0.004	0.018	0.021	0.018
NGC 6411	14.2	5.0	176.8	4.1	-0.034	0.019	0.007	0.026
NGC 6703	9.3	2.3	179.0	1.7	-0.020	0.035	-0.012	0.034
NGC 7454	10.7	4.7	117.5	3.3	0.002	0.016	-0.051	0.014
NGC 7785	67.2	16.3	229.6	8.2	0.039	0.034	-0.067	0.044

scope of this paper to explore further the variety of intrinsic structure associated with this scatter. More detailed and extensive studies of individual objects should give better insight in the future.

In contrast to $\langle H_3\rangle$, $\langle H_4\rangle$ hardly correlates with any parameter (see Fig. 16). Because one generally would expect a relation between anisotropy and $\langle H_4\rangle$, we show the corresponding plot in Fig. 16(b). If one is willing to read any dependence of $\langle H_4\rangle$ on $(v/\sigma)^*$ from this plot, then one may actually see two correlations, one for anisotropic objects ($\log(v/\sigma)^* < -0.5$) and one for rotationally flattened objects. In both cases, more rotation (respectively, less anisotropy) means more positive $\langle H_4\rangle$.

Nevertheless, as already emphasized above, there is one strong conclusion that we can draw from the absence of strongly negative $\langle H_4\rangle$ values in non-rotating ellipticals: two-integral models cannot be applied to these galaxies because they predict significantly flat-topped LOSVDs. For discy ellipticals, the necessity for a third integral is less obvious because of their two-component nature, which requires disentangling of the two components in the LOSVD (e.g. Scorza & Bender 1994) prior to modelling.

All results described in the last paragraphs referred to H_3, H_4 and v/σ measured on the major axes of the galaxies. The situation may be quite similar for their minor axis data but we are unable to demonstrate this, because the range in v/σ on the minor axes is much smaller than on the major axes and the detection of significant correlations is therefore not possible.

Table 5. Mean velocity, velocity dispersion, $\langle H_3\rangle$, $\langle H_4\rangle$ along the minor axes of the galaxies listed in Table 2 with minor axis data.

Galaxy	v $\left(\frac{\text{km}}{\text{s}}\right)$	δv $\left(\frac{\text{km}}{\text{s}}\right)$	σ_m $\left(\frac{\text{km}}{\text{s}}\right)$	$\delta\sigma_\text{m}$ $\left(\frac{\text{km}}{\text{s}}\right)$	$\langle H_3\rangle$	$\delta\langle H_3\rangle$	$\langle H_4\rangle$	$\delta\langle H_4\rangle$
NGC 1600	3.4	4.0	330.2	13.9	0.008	0.026	0.002	0.032
NGC 1700	17.2	9.2	227.3	1.0	0.033	0.047	-0.086	0.044
NGC 2300	8.9	8.2	252.2	11.3	-0.036	0.012	-0.028	0.039
NGC 3607	6.9	2.2	210.8	5.6	-0.026	0.012	0.055	0.014
NGC 3610	0.8	2.2	150.8	1.2	-0.047	0.033	-0.004	0.032
NGC 3640	1.4	2.7	195.9	2.8	-0.001	0.020	0.008	0.019
NGC 4261	48.8	8.8	268.8	7.2	0.012	0.044	-0.012	0.044
NGC 4291	14.9	8.5	260.9	17.4	-0.009	0.033	0.009	0.036
NGC 4365	29.9	3.9	237.9	5.0	-0.005	0.015	0.009	0.013
NGC 4406	17.7	3.5	222.7	4.6	0.003	0.012	0.022	0.011
NGC 4472	6.5	3.9	284.7	8.6	0.003	0.024	-0.001	0.024
NGC 4486B	5.0	5.0	172.0	24.6	0.024	0.021	-0.037	0.034
NGC 4621	1.0	1.7	207.3	7.7	0.009	0.028	0.009	0.026
NGC 4649	9.2	5.7	325.1	8.7	0.012	0.026	0.080	0.027
NGC 4660	6.4	2.3	169.0	16.7	-0.004	0.025	0.130	0.036
NGC 5322	1.7	4.9	243.6	3.0	0.000	0.014	0.020	0.014
NGC 6411	6.2	2.7	179.7	2.7	-0.003	0.015	-0.004	0.035
NGC 7785	4.9	3.0	233.2	7.9	0.007	0.017	0.011	0.015

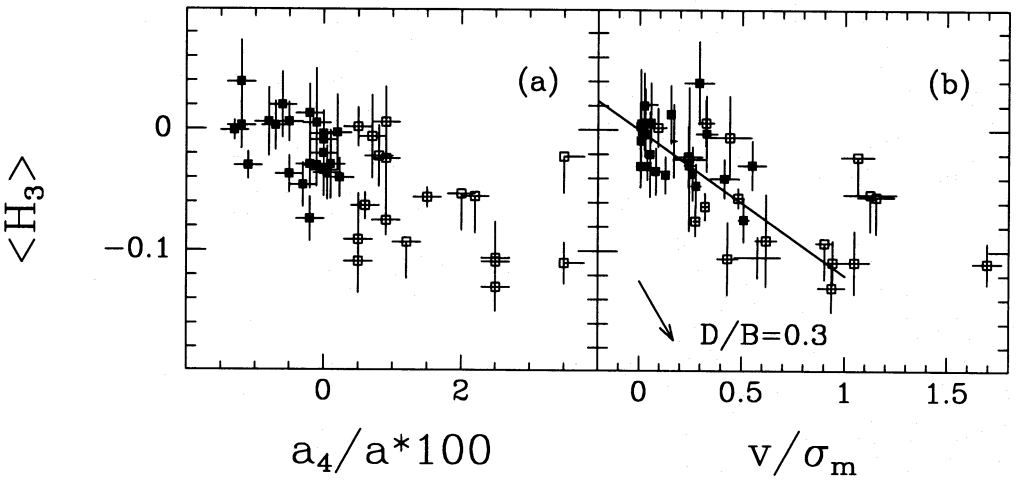

Figure 14. (a) The correlation between $\langle H_3\rangle$ and a_4/a. Filled squares are boxy objects, open squares are discy objects. If only an errorbar is shown, either the object has irregular isophotes or isophotal shapes are not known. Upper or lower limits are shown by single-sided errorbars. (b) The correlation between $\langle H_3\rangle$ and v/σ_m. Symbols as before. The arrow shows how the addition of a cold disc component of disc-to-bulge ratio 0.3 would move a point from the mean relation shown by the solid line (see equation 5).

This is a problem which can hardly be overcome by a larger sample; what is needed is much more accurate measurements than those presented here.

5.2 Correlations including radial changes in velocity dispersion

The velocity dispersion profiles of elliptical galaxies show significant individuality. Although the relative decreases in velocity dispersion along major and minor axes ($\Delta_{\sigma,\text{ma}}$, $\Delta_{\sigma,\text{mi}}$) are correlated roughly one-to-one (see Fig. 17a), significant scatter exists and indicates different kinds of velocity dispersion anisotropy for different objects. The steepest velocity dispersion profiles observed correspond to those of an isotropic Jaffe model.

While in most objects the velocity dispersion profiles decrease from the centre to the outside, some also show a local minimum close to the centre. This is observed especially in galaxies with kinematically decoupled cores (see the dispersion profiles of NGC 4494 and NGC 5322), where the minimum in velocity dispersion is associated with a larger local amplitude in rotation. This anticorrelation between dispersion and rotation is also observed in general, that is $v^2+\sigma^2$ is more nearly radially constant than either velocity dispersion or rotation velocity.

If elliptical galaxies were meridionally isotropic, then the projected velocity dispersions should be nearly constant on circles (Dehnen & Gerhard 1994). Unfortunately, we cannot decide whether the velocity dispersions are constant on ellipses or constant on circles because at about $R_\text{e}/2$ most gradients are too shallow (see also Franx et al. 1989). In most objects, the largest relative change in velocity dispersion occurs at some

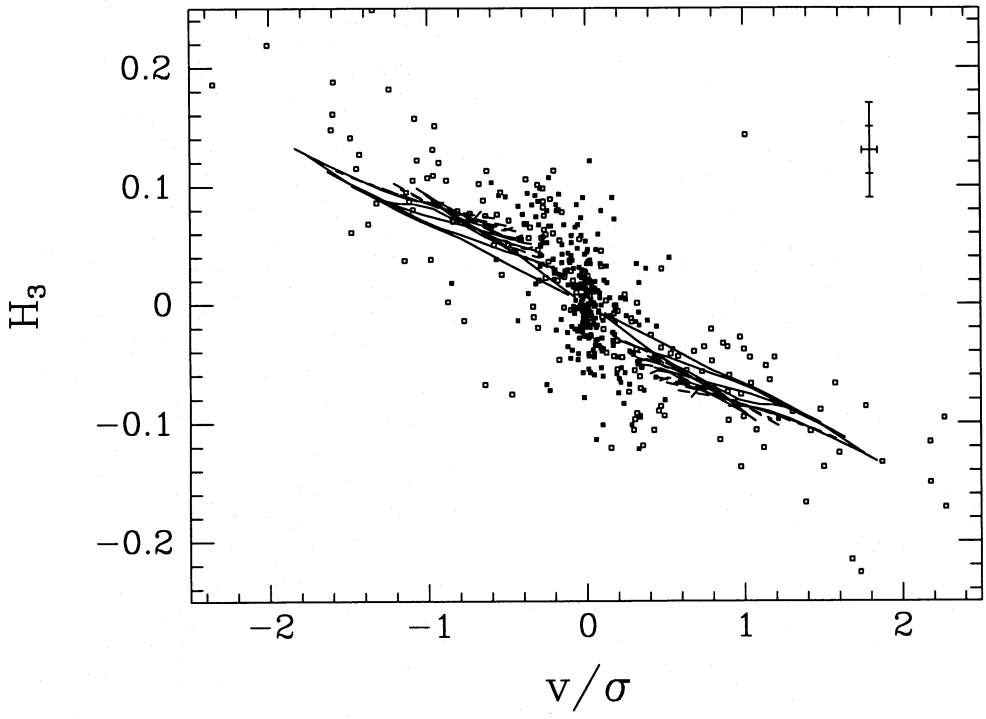

Figure 15. The *local* correlation between H_3 and v/σ within elliptical galaxies. All data points with H_3 errorbars less than 0.05 are plotted. Typical errorbars are shown in the upper right of the diagram with the bigger errorbar corresponding to larger radii and in turn larger v/σ in the galaxies. Open squares represent discy objects, filled squares all other objects. The lines show the expected $H_3 - v/\sigma$ relations for two-integral models of different flattening and inclination.

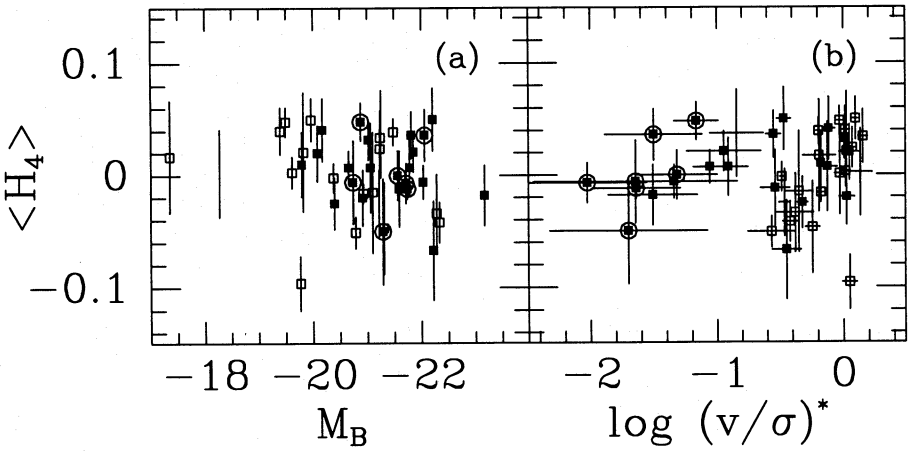

Figure 16. (a) $\langle H_4 \rangle$ against total absolute B magnitude M_B. (b) $\langle H_4 \rangle$ against anisotropy $(v/\sigma)^*$.

radius well inside $R_e/2$. This radius does not appear to be correlated with the photometric size of the core (similarly to the case of counter-rotating cores, for which the radial extent is usually much larger than the photometric core radii suggest). Neither does the relative amplitude of the change seem to be correlated with the photometric core structure.

Boxy objects have smaller relative velocity decreases (along the major axis) than discy objects; similarly, round objects have somewhat smaller σ changes than flat objects (see Fig. 17b). This is easily understood since discy (or flat) objects show in general larger rotation velocities. If rotation is taken into account, i.e. if we consider the projected kinetic energy $T_p \propto v^2 + \sigma^2$, this trend disappears.

Furthermore, within the class of *boxy* ellipticals, there is a tendency for bright objects to have flatter velocity dispersion profiles than faint objects (see Fig. 17c). A similar trend is seen between R_e(kpc) and $\Delta_{\sigma,ma}$: large boxy Es have shallower gradients. One might be tempted to interpret this trend as evidence for the progressive importance of dark haloes in massive ellipticals (as e.g. proposed by Saglia et al. 1993a), especially since generally $H_4 > 0$; however, it could well be connected also to the properties of the central cusp and anisotropy. Only measurements of σ and H_4, and proper modelling using three-integral phase-space distributions will allow us to decide which is true. Note that the correlation between relative velocity dispersion changes and absolute magnitudes is lost

for *discy* objects if again the relative change in the projected kinetic energy in azimuth $T_{\phi\phi}$ is considered, while for *boxy* objects the trend is roughly preserved due to their generally low rotation velocities.

If the different $\Delta_{\sigma,\mathrm{ma}}$ in non-rotating objects were due to different amounts or kinds of anisotropy, one would expect to find a correlation between $\langle H_4 \rangle$ and $\Delta_{\sigma,\mathrm{ma}}$. But no such correlation can be seen (Fig. 17d). Neither boxy (anisotropic) objects alone, nor the whole sample shows any significant correlation between the two quantities. So far, there are not enough theoretical models that predict how $\langle H_4 \rangle$ and $\Delta_{\sigma,\mathrm{ma}}$ inside $R_e/2$ should be related for a given density profile.

5.3 Correlations between anisotropy and photometric parameters

For completeness, we also check for our sample the already well-known relations between anisotropy and absolute magnitude (Davies et al. 1983), and between anisotropy and isophotal shape (Bender 1988b).

Davies et al. found that faint ellipticals are supported by rotation ($(v/\sigma)^* \approx 1$) while luminous ellipticals are more likely to be anisotropic ($(v/\sigma)^* < 1$). Objects with strong minor axis rotation are all highly anisotropic; they are likely to be triaxial or prolate (see Binney 1985; Franx et al. 1991). The fact that anisotropy increases with luminosity is usually attributed to increasing importance of violent relaxation (and possibly merging) over dissipation with increasing mass (Davies et al. 1983; Bender et al. 1992). The same trend between anisotropy and luminosity as observed by Davies et al. (1983) is evident for our sample (see Fig. 18).

We also confirm the relation between isophotal shape and anisotropy (Bender 1988b; see also Carter 1987; Nieto, Capaccioli & Held 1988): see Fig. 18. Discy ellipticals are, independent of luminosity, more supported by rotation than boxy ellipticals. Strong minor axis rotation is exclusively observed in slowly rotating boxy ellipticals.

Whether the observed rapid rotation of discy Es is at least partly due to the rapid rotation of the discs is still under investigation (see Scorza & Bender 1994). But discy ellipticals are likely to be on average intermediate between boxy ellipticals and S0s with respect to their anisotropy, specific angular momentum and disc-to-bulge ratios (Bender 1988b; Rix & White 1990; Scorza & Bender 1994), and also with respect to their radio and X-ray properties (Bender et al. 1989).

5.4 The Fundamental Plane of ellipticals using total kinetic energy

Faber et al. (1987) and Djorgovski & Davis (1987) found that the scaling parameters of elliptical galaxies define a two-dimensional manifold, the so-called Fundamental Plane. The existence of this plane is interpreted as a consequence of the virial theorem and the fact that elliptical galaxies have nearly constant mass-to-light ratios (e.g. Faber et al. 1987). The equation of the Fundamental Plane is

$$R_e \propto \sigma_c^{1.35} I_e^{-0.85} \quad (6)$$

with R_e being the effective radius, I_e the mean surface brightness in flux units within the effective radius and σ_c the central velocity dispersion (Faber et al. 1987; Djorgovski & Davis 1987). The observed small scatter around the Fundamental Plane represents a strong constraint on the stellar populations and internal dynamics of elliptical galaxies (e.g. Djorgovski 1992; Saglia et al. 1993b; Renzini & Ciotti 1993). The small scatter also conforms well with the relatively homogeneous and systematic properties of the LOSVDs derived here. Both facts suggest that only a rather restricted range of dynamical models is realized in elliptical galaxies.

In an equivalent representation introduced by Dressler et al. (1987), the Fundamental Plane can also be written as

$$D_n \propto \sigma_c^{1.2} \quad (7)$$

where D_n corresponds to the diameter of the isophote within which the mean effective surface brightness in the B-band equals 20.75 mag arcsec^{-2}.

One expects that, if indeed the virial theorem is the underlying reason for the existence of the Fundamental Plane, then the scatter about the plane should become smaller when the true mean kinetic energy is used instead of the central velocity dispersion (see also discussions in Djorgovski & Santiago 1993 and van der Marel 1991). We approximate the mean kinetic energy via

$$2T \propto 3\sigma_m^2 + (\frac{4}{\pi}\alpha v)^2 \quad (8)$$

where σ_m is the mean of the velocity dispersion σ_{fit} within $R_e/2$, v is the fit value of the rotation velocity, the factor $4/\pi$ compensates for the effect of randomly projecting a constant rotation velocity disc, and α denotes the correction for line profile asymmetry according to the relevant curve in Fig. 3. The corresponding corrections to σ_{fit} are small according to Fig. 3 for the line profile shapes we can measure, and are neglected.

Now, as Fig. 19 shows, use of $T^{1/2}$ instead of σ_c as defined here, or σ_{7S} as given by Davies et al. (1987), indeed results in smaller scatter about the Fundamental Plane. The rms-deviation in $T^{1/2}$ is about 20 per cent smaller than in σ_{7S}, and about 25 per cent smaller than in σ_c¶. Although expected, this result is not completely trivial. For example, if ellipticals became dark matter dominated at $R_e/2$, say, then the mean kinetic energy could show more scatter than the central velocity dispersion.

6 CONCLUSIONS

We have measured line-of-sight velocity distributions (LOSVDs) for an unbiased sample of 44 elliptical galaxies by means of the Fourier correlation quotient method. From the observed LOSVDs, fitted rotation velocities and velocity dispersions were derived and deviations of the LOSVDs from Gaussian shapes were analysed. These deviations were parametrized by the amplitudes H_3 and H_4 of the third- and fourth-order Gauss-Hermite functions. From our analysis we draw the following conclusions.

¶ Note that Davies et al. (1987) corrected their σ_{7S} to a consistent true aperture size. This correction was not applied to σ_c which may explain the somewhat larger scatter in σ_c relative to σ_{7S}.

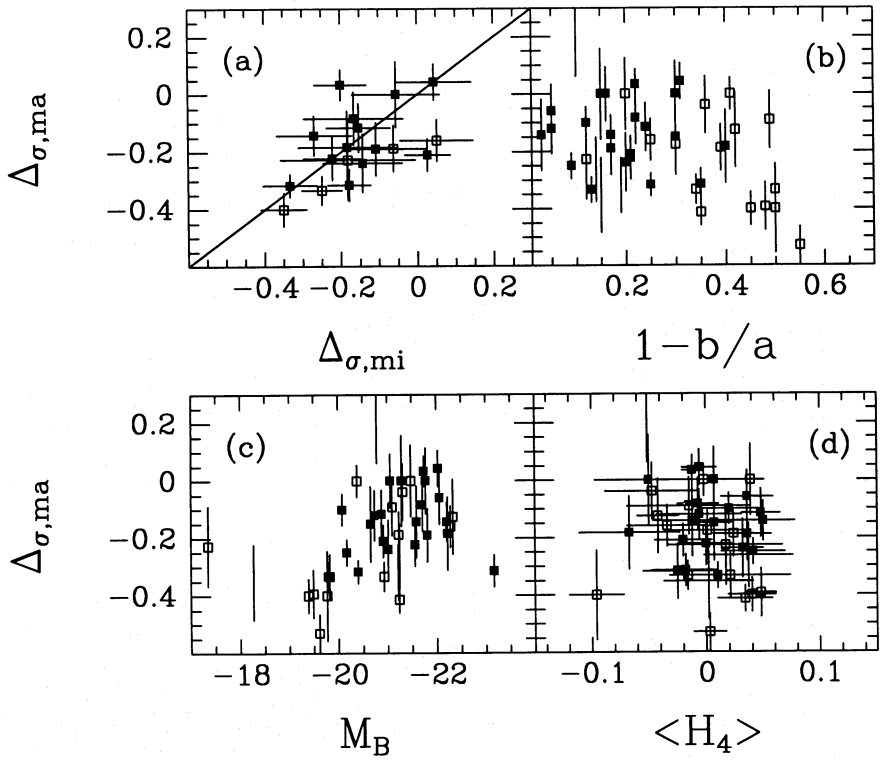

Figure 17. The relative velocity dispersion changes between the centre and $R_e/2$, measured along the major and minor axes, $\Delta_{\sigma,ma}$ and $\Delta_{\sigma,mi}$, against each other (a) and against ellipticity $1-b/a$ (b), absolute blue magnitude M_B (c), and deviation from Gaussian LOSVD $\langle H_4 \rangle$ (d). Symbols as in Fig. 14.

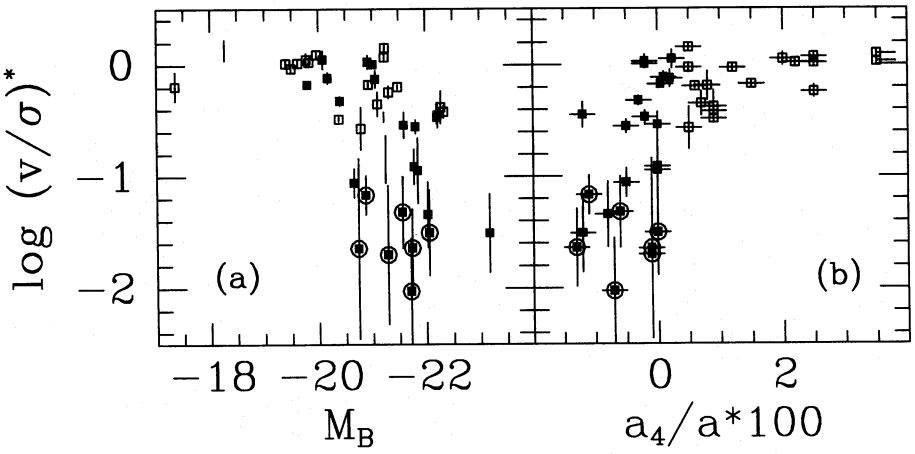

Figure 18. (a) The relation between M_B and $(v/\sigma)^*$. (b) The correlation between a_4/a and $(v/\sigma)^*$. Objects with strong minor axis rotation ($\mu \geq 0.5$) are circled. On average, anisotropy increases with luminosity. However, discy ellipticals (open squares) are mostly supported by rotation, independent of luminosity. Boxy ellipticals show a variety of anisotropies but are mostly flattened by anisotropy. Objects with $\mu \geq 0.5$ are presumably prolate or triaxial.

(1) Generally, the deviations from Gaussian LOSVDs are small (of the order of 10 per cent) with the asymmetric deviations (parametrized by H_3) being in most cases more prominent than the symmetric ones (H_4).

(2) The *asymmetric* deviations H_3 correlate well with v/σ both locally and globally (= averaged in radius), i.e. the LOSVDs of virtually all rotating objects are asymmetric. The asymmetry is of the kind that $H_3 < 0$ for $v > v_{sys}$. This means that the prograde wing is always steeper than the retrograde wing. In discy ellipticals, the presence of a rapidly rotating disc superimposed on a more slowly rotating bulge increases the asymmetry of the LOSVD, but simple modelling shows that it cannot account for the full amplitude in H_3. Nor in general can the asymmetry of the LOSVDs be explained by integration along the line of sight alone. Therefore, the LOSVDs of most rotating ellipticals/bulges must be intrinsically asymmetric.

(3) Published isotropic rotator models predict a rather tight *local* relation between H_3 and v/σ within galaxies, quite in-

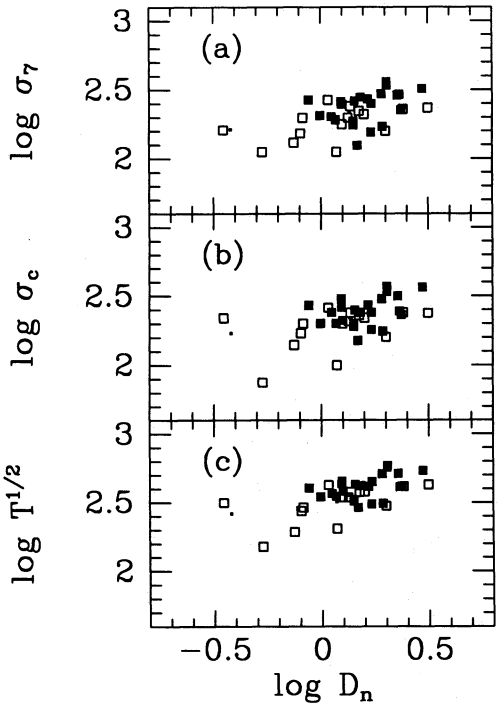

Figure 19. The Fundamental Plane using (a) velocity dispersions from Davies et al. (1987), (b) central velocity dispersions as derived here, and (c) the square root of mean kinetic energy (for definitions see text).

dependent of flattening and inclination. The mean *observed* dependence of local H_3 on local v/σ within the galaxies is different in shape and in slope from the prediction of the models, and the observed scatter is much larger. Isotropic rotator models therefore do not fit most rotating disc-free ellipticals. Discy ellipticals require a more thorough analysis before a conclusion can be drawn.

(4) Significant but smaller *symmetric* deviations of the LOSVDs from Gaussians are also detected. The observed range of symmetric deviations is $\langle H_4 \rangle = -0.05$ to $\langle H_4 \rangle = 0.05$. From the absence of strongly negative H_4 in flattened non-rotating ellipticals, we can conclude that axisymmetric two-integral models are unable to describe the dynamics of these objects either.

(5) The *detailed* study of radial profiles in v, σ, H_3 and H_4 promises to provide interesting constraints on the distribution functions of the stars in elliptical galaxies, as for example is apparent in the cases of M87 and NGC 4660. In M87, the radial H_4 profile changes from positive to negative values at about the core radius of the galaxy. This argues for radially anisotropic spherical or oblate models, because radial orbits produce a flat-top LOSVD ($H_4 < 0$) in the core and a peaked LOSVD outside ($H_4 > 0$), and qualitatively explain the observed H_4 profile in M87. On the other hand, isotropic spherical models with varying central cuspiness and face-on oblate isotropic rotator models appear inconsistent with the observed H_4 profile. In NGC 4660, the shapes of the LOSVD on both the major and minor axes can qualitatively be understood in terms of a disc+bulge model. The influence of the disc shows especially clearly along the minor axis of this galaxy where it causes strongly positive H_4 values.

(6) The velocity dispersion profiles of elliptical galaxies show significant individuality but in most objects tend to become flat outside $R_e/4$. We also investigated the well-known correlations between anisotropy, absolute magnitude and isophotal shape. We confirm previous findings: anisotropy is on average higher in more luminous ellipticals, and discy ellipticals appear to be mostly supported by rotation.

(7) We showed that the scatter about the Fundamental Plane of elliptical galaxies is reduced by 20 per cent if the mean kinetic energy is considered instead of the central velocity dispersion. This small scatter and the relatively homogeneous and systematic properties of the LOSVD shapes suggest that only a restricted range of dynamical models is realized in elliptical galaxies.

Besides providing an overview of the variety of LOSVDs observed in elliptical galaxies, we identified the following classes, also with a view to theoretical modelling: (a) spherical non-rotating Es, (b) rotating discy Es, (c) rotating boxy Es, (d) flattened Es without any rotation. The next step in the study of the dynamical structure of elliptical galaxies will now be to analyse prototypical objects of these classes in greater detail, with better signal-to-noise ratio and higher spatial and velocity resolution.

ACKNOWLEDGMENTS

We thank Claus Möllenhoff and Peter Surma for providing spectra of several objects before publication, and Walter Dehnen for discussions. We are grateful to the staff of Calar Alto Observatory for efficient support during the observations. Financial support by the Deutsche Forschungsgemeinschaft under SFB 328 and a Heisenberg fellowship (to OEG) is gratefully acknowledged. OEG also thanks the Institute for Theoretical Physics in Santa Barbara for their hospitality.

REFERENCES

Bender R., 1988a, A&A, 202, L5
Bender R., 1988b, A&A, 193, L7
Bender R., 1990, A&A, 229, 441
Bender R., Surma P., 1992, A&A, 258, 250
Bender R., Döbereiner S., Möllenhoff C., 1988, A&AS, 74, 385
Bender R., Surma P., Döbereiner S., Möllenhoff C., Madejski R., 1989, A&A, 217, 35
Bender R., Burstein D., Faber S.M., 1992, ApJ, 399, 462
Bender R., Burstein D., Faber S.M., 1993, in Hensler G. et al., eds, Panchromatic View of Galaxies: their Evolutionary Puzzle. Editions Frontières, Gif sur Yvette, in press
Bertin G. et al., 1994, submitted to A&A
Bertola F., Pizzella A., Persic M., Salucci P., 1993, ApJ, 416, L45
Binney J., 1978, MNRAS, 183, 501
Binney J., 1985, MNRAS, 212, 767
Binney J., Mamon G.A., 1982, MNRAS, 200, 361
Binney J., Davies R.L., Illingworth G.D., 1990, ApJ, 361, 78
Burstein D., Davies R.L., Dressler A., Faber S.M., Stone R.P.S., Lynden-Bell D., Terlevich R.L., Wegner G., 1987, ApJS, 64, 601
Carollo C.M., Danziger I.J., Buson L., 1993, MNRAS, 265, 553
Carter D., 1987, ApJ, 312, 514
Cinzano P., van der Marel R.P., 1993, in Danziger I.J., Zeilinger W.W., Kjär K., eds, Structure, Dynamics and Chemical Evolution of Early-Type Galaxies, ESO Conference and Workshop Proceedings No. 45. Garching bei München, p. 105

Davies R.L., 1988, in Corwin H.G. Jr, Bottinelli L., eds, Le monde du Galaxies. Springer, Berlin, p. 312
Davies R.L., Illingworth G., 1983, ApJ, 266, 516
Davies R.L., Birkinshaw M., 1988, ApJS, 68, 409
Davies R.L., Efstathiou G., Fall S.M., Illingworth G., Schechter P.L., 1983, ApJ, 266, 41
Davies R.L., Burstein D., Dressler A., Faber S.M., Lynden-Bell D., Terlevich R.J., Wegner G., 1987, ApJS, 64, 581
Davies R.L., Sadler E.M., Peletier R.F., 1993, MNRAS, 262, 650
Dehnen W., 1993, MNRAS, 265, 250
Dehnen W., Gerhard O.E., 1993, MNRAS, 261, 311
Dehnen W., Gerhard O.E., 1994, MNRAS, 268, 1019
Dejonghe H., 1987, MNRAS, 224, 13
Dejonghe H., Merritt D., 1992, ApJ, 391, 531
de Zeeuw P.T., 1985, MNRAS, 216, 273
Djorgovski S., 1992, in de Carvalho R.R., Cosmology and Large-Scale Structure in the Universe, ASP Conf. Ser. Vol. 24. Astron. Soc. Pac., San Francisco, p. 19
Djorgovski S., Davis M., 1987, ApJ, 313, 59
Djorgovski S., Santiago B.X., 1993, in Danziger I.J., Zeilinger W.W., Kjär K., eds, Structure, Dynamics and Chemical Evolution of Early-Type Galaxies, ESO Conference and Workshop Proceedings No. 45. Garching bei München, p. 59
Dressler A., Richstone D.O., 1990, ApJ, 348, 120
Dressler A., Lynden-Bell D., Burstein D., Davies R.L., Faber S.M., Terlevich R.J., Wegner G., 1987, ApJ, 313, 42
Evans N.W., 1993, MNRAS, 260, 191
Evans N.W., 1994, MNRAS, 267, 333
Faber S.M., Dressler A., Davies R.L., Burstein D., Lynden-Bell D., Terlevich R., Wegner G., 1987, in Faber S.M., ed., Nearly Normal Galaxies, From the Planck Time to the Present. Springer Verlag, New York, p. 175
Faber S.M., Wegner G., Burstein D., Davies R.L., Davies R.L., Dressler A., Lynden-Bell D., Terlevich R., 1989, ApJS, 69, 763
Franx M., Illingworth G., 1988, ApJ, 327, L55
Franx M., Illingworth G., Heckman T., 1989, ApJ, 344, 613
Franx M., Illingworth G., de Zeeuw P.T., 1991, ApJ, 383, 112
Fried J.W., Illingworth G.D., 1994, AJ, 107, 992
Gerhard O.E., 1991, MNRAS, 250, 812
Gerhard O.E., 1993, MNRAS, 265, 213
Hunter C., de Zeeuw P.T., 1992, ApJ, 389, 79
Illingworth G.D., Schechter P.L., 1982, ApJ, 256, 481
Jaffe W., Ford H.C., Ferrarese L., Vandenbosch F., O'Connell R.W., 1993, Nat, 364, 212
Jedrzejewski R.I., Schechter P.L., 1988, ApJ, 330, L87
Jedrzejewski R.I., Schechter P.L., 1989, AJ, 98, 147
Kent, S.M., 1990, in Kron R.G., ed., Evolution of the Universe of Galaxies, ASP Conf. Ser. Vol. 10. Astron. Soc. Pac., San Francisco, p. 109
Kormendy J., 1982, ApJ, 257, 75
Kormendy J., 1985, ApJ, 292, L9
Kormendy J., 1993, in Beckman J.E., Netzer H., Colina L., eds, The Nearest Active Galaxies. Madrid, in press
Kormendy J., Illingworth G., 1982, ApJ, 256, 460
Kormendy J., Richstone D., 1992, ApJ, 393, 559
Kuijken K., Merrifield M.R., 1993, MNRAS, 264, 712
Laird J.B., Levison H.F., 1985, AJ, 90, 2652
Lauer T.R. et al., 1992, AJ, 103, 703
Merrifield M.R., Kent S.M., 1990, AJ, 99, 1548
Merritt D., 1987, ApJ, 319, 55
Merritt D., 1993, ApJ, 413, 79
Möllenhoff C., Bender R., 1987, A&A, 174, 63
Nieto J.L., Capaccioli M., Held E., 1988, A&A, 195, L1
Renzini A., Ciotti L., 1993, ApJ, 416, L49
Richstone D.O., Bower G., Dressler A., 1990, ApJ, 353, 118
Rix H-W., White S.D.M., 1990, ApJ, 362, 52
Rix H-W., White S.D.M., 1992, MNRAS, 254, 389
Saglia R.P., Bertin G., Bertola F., Danziger I.J., Sadler E.M., Stiavelli M., Zeilinger W.W., de Zeeuw T., 1993a, ApJ, 403, 567
Saglia R.P., Bender R., Dressler A., 1993b, A&A, 279, 75
Saha P., Williams T.B., 1994, AJ, 107, 1295
Sandage A., Tammann G.A., 1987, A revised Shapley-Ames Catalogue of Bright Galaxies. Carnegie Institution of Washington Publications, Washington
Sargent W.L.W., Schechter P.L., Boksenberg A., Shortridge K., 1977, ApJ, 212, 326
Sargent W.L.W., Young P.J., Boksenberg A., Shortridge K., Lynds C.R., Hartwick F.D.A., 1978, ApJ, 221, 731
Scorza C., Bender R., 1994, A&A, in press
Solf J., 1983, MPI Astronomie Users manual
Surma P., 1992, PhD Thesis, Universität Heidelberg
van der Marel R., 1991, MNRAS, 253, 710
van der Marel R., Franx M., 1993, ApJ, 407, 525
van der Marel R., Rix H.-W., Carter D., Franx M., White S.D.M., de Zeeuw T., 1994, MNRAS, 268, 521
Wagner S.J., Dettmar R.-J., Bender R., 1989, A&A, 215, 243
Winsall M.L., Freeman K.C., 1993, A&A, 268, 443
Worthey G., Faber S.M., Gonzales J.J., 1992, ApJ, 398, 69

This paper has been produced using the Blackwell Scientific Publications LaTeX style file.